



HAL
open science

The Sloan Digital Sky Survey Reverberation Mapping Project: $H\alpha$ and $H\beta$ Reverberation Measurements from First-year Spectroscopy and Photometry

C. J. Grier, J. R. Trump, Yue Shen, Keith Horne, Karen Kinemuchi, Ian D. Mcgreer, D. A. Starkey, W. N. Brandt, P. B. Hall, C. S. Kochanek, et al.

► **To cite this version:**

C. J. Grier, J. R. Trump, Yue Shen, Keith Horne, Karen Kinemuchi, et al.. The Sloan Digital Sky Survey Reverberation Mapping Project: $H\alpha$ and $H\beta$ Reverberation Measurements from First-year Spectroscopy and Photometry. *Astrophys.J.*, 2017, 851 (1), pp.21. 10.3847/1538-4357/aa98dc . hal-01669686

HAL Id: hal-01669686

<https://hal.science/hal-01669686>

Submitted on 14 Apr 2018

HAL is a multi-disciplinary open access archive for the deposit and dissemination of scientific research documents, whether they are published or not. The documents may come from teaching and research institutions in France or abroad, or from public or private research centers.

L'archive ouverte pluridisciplinaire **HAL**, est destinée au dépôt et à la diffusion de documents scientifiques de niveau recherche, publiés ou non, émanant des établissements d'enseignement et de recherche français ou étrangers, des laboratoires publics ou privés.



The Sloan Digital Sky Survey Reverberation Mapping Project: $H\alpha$ and $H\beta$ Reverberation Measurements from First-year Spectroscopy and Photometry

C. J. Grier^{1,2} , J. R. Trump^{1,3} , Yue Shen^{4,5,34} , Keith Horne⁶ , Karen Kinemuchi⁷ , Ian D. McGreer⁸ , D. A. Starkey⁶,
W. N. Brandt^{1,2,9} , P. B. Hall¹⁰ , C. S. Kochanek^{11,12} , Yuguang Chen¹³, K. D. Denney^{11,12,14}, Jenny E. Greene¹⁵,
L. C. Ho^{16,17} , Y. Homayouni³, Jennifer I-Hsiu Li⁴, Liuyi Pei⁴, B. M. Peterson^{11,12,18} , P. Petitjean¹⁹, D. P. Schneider^{1,2},
Mouyuan Sun²⁰ , Yusura AlSayyad¹⁵, Dmitry Bizyaev^{7,21} , Jonathan Brinkmann⁷, Joel R. Brownstein²² , Kevin Bundy²³ ,
K. S. Dawson²² , Sarah Eftekharzadeh²⁴, J. G. Fernandez-Trincado^{25,26}, Yang Gao²⁷ , Timothy A. Hutchinson²² , Siyao Jia²⁸,
Linhua Jiang¹⁶ , Daniel Oravetz⁷, Kaike Pan⁷ , Isabelle Paris²⁹, Kara A. Ponder³⁰ , Christina Peters³¹, Jesse Rogerson³² ,
Audrey Simmons⁷ , Robyn Smith³³, and and Ran Wang¹⁶

¹ Dept. of Astronomy and Astrophysics, The Pennsylvania State University, 525 Davey Laboratory, University Park, PA 16802, USA

² Institute for Gravitation and the Cosmos, The Pennsylvania State University, University Park, PA 16802, USA

³ Department of Physics, University of Connecticut, 2152 Hillside Road, Unit 3046, Storrs, CT 06269, USA

⁴ Department of Astronomy, University of Illinois at Urbana-Champaign, Urbana, IL 61801, USA

⁵ National Center for Supercomputing Applications, University of Illinois at Urbana-Champaign, Urbana, IL 61801, USA

⁶ SUPA Physics and Astronomy, University of St Andrews, Fife, KY16 9SS, Scotland, UK

⁷ Apache Point Observatory and New Mexico State University, P.O. Box 59, Sunspot, NM, 88349-0059, USA

⁸ Steward Observatory, The University of Arizona, 933 North Cherry Avenue, Tucson, AZ 85721, USA

⁹ Department of Physics, 104 Davey Lab, The Pennsylvania State University, University Park, PA 16802, USA

¹⁰ Department of Physics and Astronomy, York University, Toronto, ON M3J 1P3, Canada

¹¹ Department of Astronomy, The Ohio State University, 140 West 18th Avenue, Columbus, OH 43210, USA

¹² Center for Cosmology and AstroParticle Physics, The Ohio State University, 191 West Woodruff Avenue, Columbus, OH 43210, USA

¹³ Cahill Center for Astronomy and Astrophysics, California Institute of Technology, 1200 East California Boulevard, MC 249-17, CA 91125, USA

¹⁴ Illumination Works, LLC, 5550 Blazer Parkway, Dublin, OH, 43017, USA

¹⁵ Department of Astrophysical Sciences, Princeton University, Princeton, NJ 08544, USA

¹⁶ Kavli Institute for Astronomy and Astrophysics, Peking University, Beijing 100871, China

¹⁷ Department of Astronomy, School of Physics, Peking University, Beijing 100871, China

¹⁸ Space Telescope Science Institute, 3700 San Martin Drive, Baltimore, MD 21218, USA

¹⁹ Institut d'Astrophysique de Paris, Université Paris 6-CNRS, UMR7095, 98bis Boulevard Arago, F-75014 Paris, France

²⁰ Key Laboratory for Research in Galaxies and Cosmology, Center for Astrophysics, Department of Astronomy,
University of Science and Technology of China, Chinese Academy of Sciences, Hefei, Anhui 230026, China

²¹ Sternberg Astronomical Institute, Moscow State University, Moscow, Russia

²² Department of Physics and Astronomy, University of Utah, 115 South 1400 East, Salt Lake City, UT 84112, USA

²³ UCO/Lick Observatory, University of California, Santa Cruz, 1156 High St., Santa Cruz, CA 95064, USA

²⁴ Department of Physics and Astronomy, University of Wyoming, Laramie, WY 82071, USA

²⁵ Departamento de Astronomía, Casilla 160-C, Universidad de Concepción, Concepción, Chile

²⁶ Institut Utinam, CNRS UMR6213, Univ. Bourgogne Franche-Comté, OSU THETA, Observatoire de Besançon, BP 1615, 25010 Besançon Cedex, France

²⁷ Department of Engineering Physics and Center for Astrophysics, Tsinghua University, Beijing 100084, China; Key Laboratory of Particle and Radiation Imaging
(Tsinghua University), Ministry of Education, Beijing 100084, China

²⁸ Department of Astronomy, University of California, Berkeley, CA 94720, USA

²⁹ Aix-Marseille Université, CNRS, LAM (Laboratoire d'Astrophysique de Marseille) UMR 7326, F-13388, Marseille, France

³⁰ Pittsburgh Particle Physics, Astrophysics, and Cosmology Center (PITT PACC), Physics and Astronomy Department,
University of Pittsburgh, Pittsburgh, PA 15260, USA

³¹ Dunlap Institute & Department of Astronomy and Astrophysics, University of Toronto, 50 St George Street, Toronto, ON M5S 3H4, Canada

³² Canada Aviation and Space Museum, 11 Aviation Parkway, Ottawa, ON, K1K 4Y5, Canada

³³ Department of Astronomy, University of Maryland, Stadium Drive, College Park, MD 20742-2421, USA

Received 2017 April 25; revised 2017 October 3; accepted 2017 October 14; published 2017 December 7

Abstract

We present reverberation mapping results from the first year of combined spectroscopic and photometric observations of the Sloan Digital Sky Survey Reverberation Mapping Project. We successfully recover reverberation time delays between the $g+i$ band emission and the broad $H\beta$ emission line for a total of 44 quasars, and for the broad $H\alpha$ emission line in 18 quasars. Time delays are computed using the JAVELIN and CREAM software and the traditional interpolated cross-correlation function (ICCF): using well-defined criteria, we report measurements of 32 $H\beta$ and 13 $H\alpha$ lags with JAVELIN, 42 $H\beta$ and 17 $H\alpha$ lags with CREAM, and 16 $H\beta$ and eight $H\alpha$ lags with the ICCF. Lag values are generally consistent among the three methods, though we typically measure smaller uncertainties with JAVELIN and CREAM than with the ICCF, given the more physically motivated light curve interpolation and more robust statistical modeling of the former two methods. The median redshift of our $H\beta$ -detected sample of quasars is 0.53, significantly higher than that of the previous reverberation mapping sample. We find that in most objects, the time delay of the $H\alpha$ emission is consistent with or slightly longer than that of $H\beta$. We measure black hole masses using our measured time delays and line widths for these quasars. These black hole mass measurements are mostly consistent with expectations based on the local $M_{\text{BH}}-\sigma_*$ relationship, and are also consistent with single-epoch black hole mass measurements. This work increases the current sample size of reverberation-mapped active galaxies by about two-thirds and represents the first large sample of reverberation mapping observations beyond the local universe ($z < 0.3$).

³⁴ Alfred P. Sloan Research Fellow.

Key words: galaxies: active – galaxies: nuclei – quasars: emission lines – quasars: general

Supporting material: figure sets, machine-readable tables

1. Introduction

Over the past few decades, the technique of reverberation mapping (RM; e.g., Blandford & McKee 1982; Peterson et al. 2004) has emerged as a powerful tool for measuring black hole masses (M_{BH}) in active galactic nuclei (AGNs). RM allows a measurement of the size of the broad-line-emitting region (BLR), which is photoionized by continuum emission from closer to the black hole (BH). Variability of the continuum is echoed by the BLR after a time delay that corresponds to the light travel time between the continuum-emitting region and the BLR; this time delay provides a measurement of the distance between the two regions and thus a characteristic size for the BLR (R_{BLR}).

Assuming that the motion of the BLR gas is dominated by the gravitational field of the central BH, we can combine R_{BLR} with the broad-emission-line width (ΔV) to measure a BH mass of

$$M_{\text{BH}} = \frac{f R_{\text{BLR}} \Delta V^2}{G}, \quad (1)$$

where the dimensionless scale factor f accounts for the orientation, kinematics, and structure of the BLR.

Thus far, about 60 AGNs have M_{BH} measurements obtained through reverberation mapping (e.g., Kaspi et al. 2000, 2005; Peterson et al. 2004; Bentz et al. 2009, 2010; Denney et al. 2010; Grier et al. 2012; Du et al. 2014, 2016a, 2016b; Barth et al. 2015; Hu et al. 2015). Bentz & Katz (2015) provide a running compilation of these measurements.³⁵ Due to the stringent observational requirements of RM measurements, the existing sample is mainly composed of nearby ($z < 0.3$), lower-luminosity AGNs that have sufficiently short time delays to be measurable with a few months of monitoring using a modest-sized telescope. Because they are low redshift, these studies typically focus on the $H\beta$ emission line and other nearby lines in the observed-frame optical.

RM measurements have established the radius–luminosity (R – L) relationship (e.g., Kaspi et al. 2007; Bentz et al. 2013), which allows one to estimate the BLR size with a single spectrum and thus estimate M_{BH} for large numbers of quasars at greater distances where traditional RM campaigns are impractical (e.g., Shen et al. 2011). However, the current RM sample may be biased; beyond the fact that these AGNs are low redshift, they do not span the full range of AGN emission-line properties (see Figure 1 of Shen et al. 2015a). In addition, the R – L relation is only well calibrated for $H\beta$, but most higher-redshift, single-epoch M_{BH} estimates are made using C IV or Mg II. There are only a handful of RM measurements for C IV, particularly at high redshift (e.g., Kaspi et al. 2007), and only a few reliable Mg II lag measurements have been reported (Metzroth et al. 2006; Shen et al. 2016b). Such measurements are difficult to make because higher-luminosity quasars have longer time delays and larger time dilation factors and thus require observations spanning years rather than months.

The Sloan Digital Sky Survey Reverberation Mapping Project (SDSS-RM) is a dedicated multiobject RM program that began in

2014 (see Shen et al. 2015a for details). The major goals of this program are to expand the number of reverberation-mapped AGNs, the range of AGN parameters spanned by the RM sample, and the redshift and luminosity range of the RM sample, and to firmly establish R – L relationships for C IV and Mg II. SDSS-RM started as an ancillary program of the SDSS-III survey (Eisenstein et al. 2011) on the SDSS 2.5 m telescope (Gunn et al. 2006), monitoring 849 quasars in a single field with the Baryon Oscillation Spectroscopic Survey (BOSS) spectrograph (Dawson et al. 2013; Smee et al. 2013). Additional photometric data were acquired with the 3.6 m Canada–France–Hawaii Telescope (CFHT) and the Steward Observatory 2.3 m Bok telescope to improve the cadence of the continuum light curves. Observations for the program have continued in 2015–2017 as part of SDSS-IV (Blanton et al. 2017) to extend the temporal baseline of the program.

While the primary goals of this program are to obtain RM measurements for $\gtrsim 100$ quasars, we have been pursuing a wide variety of ancillary science goals as well, ranging from studies of emission-line and host-galaxy properties to the variability of broad absorption lines (Grier et al. 2015; Matsuoka et al. 2015; Shen et al. 2015b, 2016a; Sun et al. 2015; Denney et al. 2016). The first RM results from this program were reported by Shen et al. (2016b), who measured emission-line lags in the $H\beta$ and Mg II emission lines in 15 of the brightest, relatively low-redshift sources in our sample using the first year of SDSS-RM spectroscopy alone (i.e., no photometric data were used). Li et al. (2017) also measured composite RM lags using a low-luminosity subset and the first year of spectroscopy.

We here report results based on the combined spectroscopic and imaging data from the first year of observations, focusing on the $H\beta$ and $H\alpha$ emission lines in the low-redshift ($z < 1.1$) subset of the SDSS-RM sample. We detect significant lags in about 20% of our sample. In Section 2, we describe the sample of quasars in our study, present details of the data, and discuss data preparation. We discuss our time-series analysis methods in Section 3 and our results in Section 4, and we summarize our findings in Section 5. Throughout this work, we adopt a Λ CDM cosmology with $\Omega_{\Lambda} = 0.7$, $\Omega_M = 0.3$, and $h = 0.7$.

2. Data and Data Processing

2.1. The Quasar Sample

We selected our objects from the full SDSS-RM quasar sample, which is flux-limited ($i < 21.7$; measurements by Ahn et al. 2014) and contains 849 quasars with redshifts of $0.1 < z < 4.5$. A complete description of the parent sample and the properties of the quasars will be reported by Y. Shen et al. (2017, in preparation). Within the full sample, there are 222 quasars in the $0.11 < z < 1.13$ redshift range that places $H\beta$ in the wavelength range of the SDSS spectra. Basic information on these quasars is given in Table 1, including several spectral measurements made by Shen et al. (2015b). Figure 1 presents the distributions of the quasars in redshift, magnitude, typical spectral signal-to-noise ratio (S/N), and luminosity. Of the 222 quasars, 55 are at low-enough redshifts ($z < 0.6$) for $H\alpha$ to fall within the observed wavelength range of the spectra as well.

³⁵ <http://www.astro.gsu.edu/AGNmass/>

Table 1
Quasar Sample Information

RMID	SDSS Identifier	R.A. ^a (deg) (J2000)	Decl. ^a (deg) (J2000)	z^a	i mag ^a	MED ^b S/N	AGN $\log \lambda_{\lambda 5100}^c$ (erg s ⁻¹)	Host $\log \lambda_{\lambda 5100}^c$ (erg s ⁻¹)	$\log M_{\text{BH,SE}}^c$ (M_{\odot})
005	J141541.41+530424.3	213.9225	53.0734	1.020	20.716	5.0	44.5	...	8.1
009	J141359.51+531049.3	213.4980	53.1804	0.898	20.473	4.3	44.1	43.8	7.9
016	J141606.95+530929.8	214.0290	53.1583	0.848	19.716	11.5	44.8	43.9	9.0
017	J141324.28+530527.0	213.3511	53.0908	0.456	19.213	14.1	43.9	44.2	8.4
018	J141323.27+531034.3	213.3469	53.1762	0.849	20.205	5.2	44.3	44.2	8.9
020	J141411.66+525149.0	213.5486	52.8636	1.124	21.529	2.0
021	J141314.97+530139.4	213.3124	53.0276	1.026	21.167	3.0	44.5	44.0	7.6
027	J141600.80+525255.5	214.0033	52.8821	1.023	20.968	2.1	44.4	44.2	8.5
029	J141310.71+525750.2	213.2946	52.9640	0.816	21.142	2.6	43.8	43.7	7.7
033	J141532.36+524905.9	213.8848	52.8183	0.715	20.490	6.6	44.1	43.9	7.6
040	J141648.89+530903.6	214.2037	53.1510	0.600	20.868	3.4	43.5	43.5	7.1
050	J141522.54+524421.5	213.8439	52.7393	0.526	20.818	4.3	43.6	43.7	8.2
053	J141222.76+530648.6	213.0948	53.1135	0.894	21.361	2.8	44.0	44.0	8.0
061	J141559.99+524416.1	214.0000	52.7378	0.983	21.379	3.3	44.4	44.2	8.1
062	J141417.69+532810.8	213.5737	53.4697	0.808	20.528	4.2	44.0	44.0	8.6
077	J141747.02+530349.7	214.4459	53.0638	0.914	21.124	2.7	44.0	43.8	7.8
078	J141154.17+531119.5	212.9757	53.1887	0.581	20.134	13.3	44.4	...	8.8
085	J141539.59+523727.9	213.9150	52.6244	0.237	18.563	18.5	43.3	43.5	8.1
088	J141151.78+525344.1	212.9657	52.8956	0.516	19.731	10.9	44.1	43.7	8.5
090	J141144.12+531508.6	212.9338	53.2524	0.923	20.753	1.3	43.8	44.4	8.8
101	J141214.20+532546.7	213.0592	53.4296	0.458	18.837	21.3	44.4	43.4	7.9
102	J141352.99+523444.2	213.4708	52.5790	0.860	19.536	14.4	44.7	...	8.0
103	J141155.26+524733.6	212.9802	52.7927	0.517	19.928	4.8	43.7	44.1	9.2
111	J141626.48+533406.5	214.1104	53.5685	1.133	20.524	3.4
118	J141412.78+523209.0	213.5533	52.5358	0.714	19.318	21.2	44.8	...	8.3
121	J141125.70+524924.2	212.8571	52.8234	0.968	21.300	3.3	44.3	43.8	8.0
122	J141628.70+523346.4	214.1196	52.5629	0.986	20.933	5.0	44.6	44.4	8.1
123	J141837.85+531017.6	214.6577	53.1716	0.889	20.440	6.7	44.5	...	8.6
125	J141149.92+532721.1	212.9580	53.4559	1.076	21.524	2.4
126	J141408.76+533938.3	213.5365	53.6606	0.192	18.561	20.7	43.3	43.5	7.3
133	J141731.59+533224.4	214.3816	53.5401	0.981	20.531	5.7	44.4	44.0	7.8
134	J141054.58+531532.9	212.7274	53.2591	0.964	19.825	11.1	44.8	44.1	8.3
140	J141856.21+531007.1	214.7342	53.1687	0.609	20.162	5.3	43.8	44.0	7.5
141	J141324.66+522938.2	213.3527	52.4939	0.812	20.551	3.9	44.2	43.9	8.7
160	J141041.25+531849.0	212.6719	53.3136	0.359	19.679	9.0	43.8	...	8.2
165	J141804.59+523745.0	214.5191	52.6292	1.086	21.175	3.5
168	J141723.39+523153.9	214.3474	52.5316	0.484	21.137	2.4	43.0	43.5	7.2
171	J141321.13+534344.7	213.3380	53.7291	0.790	20.992	3.4	44.0	43.7	7.5
173	J141147.60+523414.6	212.9483	52.5707	0.970	19.917	10.1	44.8	44.4	9.0
175	J141531.32+522407.8	213.8805	52.4022	0.819	21.301	2.9	44.0	43.9	7.9
177	J141724.59+523024.9	214.3525	52.5069	0.482	19.560	10.8	44.0	43.8	8.4
184	J141721.80+534102.6	214.3408	53.6841	0.193	17.857	30.0	43.7	43.4	7.2
185	J141735.95+523029.9	214.3998	52.5083	0.987	19.889	8.1	44.8	...	8.9
187	J141005.21+531003.9	212.5217	53.1677	0.997	21.119	1.2	43.9	44.4	9.1
191	J141645.58+534446.8	214.1899	53.7463	0.442	20.448	6.2	43.6	43.6	7.5
192	J141649.44+522531.0	214.2060	52.4253	1.024	19.971	6.8	45.0	...	8.5
193	J141542.16+522207.0	213.9257	52.3686	1.003	20.498	7.2	44.8	44.0	7.7
203	J141811.34+533808.6	214.5473	53.6357	0.977	20.583	5.3	44.4	...	8.2
204	J141221.73+522556.6	213.0906	52.4324	0.922	18.575	20.6	45.1	...	8.7
211	J141522.01+535033.5	213.8417	53.8426	0.971	19.448	8.9	44.7	44.3	8.2
215	J141952.23+531340.9	214.9676	53.2280	0.884	21.290	3.6	44.2	...	8.7
229	J141018.04+532937.5	212.5752	53.4937	0.470	20.271	4.7	43.6	43.5	8.0
232	J141651.26+522046.1	214.2136	52.3461	0.807	20.776	3.8	44.0	44.1	7.6
235	J141111.30+534029.4	212.7971	53.6748	0.785	19.872	10.0	44.4	43.9	8.4
240	J141420.87+521629.9	213.5870	52.2750	0.762	20.879	3.6	43.9	44.3	8.5
243	J140924.89+530002.7	212.3537	53.0007	0.659	20.036	8.3	44.3	43.6	8.5
252	J141751.14+522311.1	214.4631	52.3864	0.281	19.768	7.1	42.7	43.5	8.6
255	J141525.41+535508.2	213.8559	53.9189	0.992	21.471	2.0	44.2	44.4	8.2
258	J142027.51+530454.5	215.1146	53.0818	0.994	20.762	2.3	44.4	43.9	8.5
260	J141018.04+523446.1	212.5752	52.5795	0.995	21.636	15.5	45.0	43.7	8.1
265	J142023.88+531605.1	215.0995	53.2681	0.734	20.645	6.8	44.2	44.0	8.3
267	J141112.72+534507.1	212.8030	53.7520	0.587	19.623	10.5	44.1	43.9	7.9

Table 1
(Continued)

RMID	SDSS Identifier	R.A. ^a	Decl. ^a			MED ^b S/N	AGN	Host	log $M_{\text{BH,SE}}^c$ (M_{\odot})
		(deg) (J2000)	(deg) (J2000)	z^a	i mag ^a		log $\lambda L_{\lambda 5100}^c$ (erg s ⁻¹)	log $\lambda L_{\lambda 5100}^c$ (erg s ⁻¹)	
268	J141043.36+534111.8	212.6807	53.6866	0.650	20.718	3.9	43.7	44.0	8.5
270	J140943.01+524153.1	212.4292	52.6981	0.421	20.095	3.7	43.5	43.6	8.3
272	J141625.71+535438.5	214.1071	53.9107	0.263	18.822	23.2	43.9	...	7.8
274	J141949.82+533033.5	214.9576	53.5093	0.793	20.546	4.9	44.3	44.0	8.3
277	J141409.44+535648.2	213.5393	53.9467	0.825	20.649	3.8	44.0	44.1	7.8
278	J141717.07+521751.5	214.3211	52.2976	1.022	20.587	5.4	44.8	...	8.5
285	J141650.92+521528.6	214.2122	52.2579	1.034	21.300	3.3
290	J141138.06+534957.7	212.9086	53.8327	1.078	19.865	7.5
291	J141643.24+521435.8	214.1802	52.2433	0.531	19.825	4.4	43.9	43.3	8.6
296	J141838.35+522359.3	214.6598	52.3998	1.120	18.750	22.6
297	J141002.21+533730.2	212.5092	53.6251	1.026	20.566	3.8	44.5	43.6	7.9
300	J141941.11+533649.6	214.9213	53.6138	0.646	19.491	16.5	44.5	44.0	8.2
301	J142010.25+524029.6	215.0427	52.6749	0.548	19.764	8.3	44.1	43.7	8.5
302	J140850.91+525750.9	212.2121	52.9642	0.981	20.954	3.1	44.3	44.1	8.3
303	J141830.20+522212.5	214.6259	52.3701	0.820	20.882	4.0	44.0	44.0	8.3
305	J141004.27+523141.0	212.5178	52.5281	0.527	19.505	11.3	44.2	43.7	7.9
306	J141622.95+521212.2	214.0956	52.2034	1.123	20.389	3.2
308	J141302.60+535729.9	213.2608	53.9583	1.130	20.815	2.7
316	J142052.44+525622.4	215.2185	52.9396	0.676	18.028	34.0	45.0	...	8.5
320	J142038.52+532416.5	215.1605	53.4046	0.265	19.467	14.4	43.4	43.4	8.1
323	J141123.22+535204.2	212.8467	53.8678	0.804	21.104	2.5	43.6	44.1	7.8
324	J141658.28+521205.1	214.2428	52.2014	0.602	19.857	13.2	44.3	43.8	8.8
328	J141313.27+535944.0	213.3053	53.9956	1.076	19.897	13.5
329	J141659.76+535806.7	214.2490	53.9685	0.720	18.107	34.8	45.2	...	8.2
331	J142107.76+530318.2	215.2823	53.0551	0.735	21.332	2.8	43.9	43.8	8.6
333	J141633.35+521001.1	214.1389	52.1670	1.089	20.811	3.8
336	J141514.15+540222.9	213.8089	54.0397	0.849	20.770	4.3	44.3	43.9	8.6
337	J142103.30+531822.4	215.2638	53.3062	0.708	20.899	2.7	43.6	44.0	8.4
338	J141955.62+534007.2	214.9818	53.6687	0.418	20.084	5.6	43.4	43.6	8.4
341	J141500.38+520658.6	213.7516	52.1163	0.424	18.562	24.8	44.4	...	8.2
350	J141914.50+534810.6	214.8104	53.8029	0.860	21.235	2.4	43.9	43.9	7.8
354	J141957.27+534157.9	214.9887	53.6994	1.111	21.306	1.9
355	J141712.97+520957.5	214.3040	52.1660	0.753	20.945	2.8	43.5	44.0	8.3
356	J141533.89+520558.0	213.8912	52.0995	0.986	18.724	30.5	45.3	...	8.5
369	J141304.34+520659.3	213.2681	52.1165	0.719	20.252	6.0	44.1	43.8	8.3
370	J142021.37+533900.8	215.0890	53.6502	0.883	21.372	3.2	44.0	43.9	8.5
371	J141123.42+521331.7	212.8476	52.2255	0.472	19.571	9.5	44.1	...	8.1
373	J141859.75+521809.7	214.7490	52.3027	0.884	19.626	12.6	44.9	...	8.8
375	J141530.66+520439.5	213.8777	52.0776	0.647	19.718	13.3	44.5	...	8.7
376	J140814.29+531855.8	212.0596	53.3155	0.933	21.148	2.4	44.4	...	7.8
377	J142043.53+523611.4	215.1814	52.6032	0.337	19.767	7.3	43.4	43.6	7.9
378	J141320.05+520527.9	213.3335	52.0911	0.600	19.851	4.2	43.8	43.9	7.9
382	J140801.35+530915.9	212.0056	53.1544	0.837	21.035	1.9	43.9	44.0	8.8
385	J142124.36+532312.5	215.3515	53.3868	0.826	21.278	3.1	44.0	44.0	8.0
392	J142112.29+524147.3	215.3012	52.6965	0.843	20.443	6.4	44.3	44.0	8.2
393	J141048.58+535605.2	212.7024	53.9348	0.583	20.519	4.2	43.9	43.7	7.5
399	J141031.33+521533.8	212.6305	52.2594	0.608	20.142	6.6	44.0	44.1	8.1
407	J142115.76+533128.7	215.3157	53.5246	0.922	19.830	8.3	44.7	43.1	8.1
421	J140822.72+533437.2	212.0947	53.5770	0.791	21.248	1.3	43.6	44.0	8.4
422	J140739.17+525850.7	211.9132	52.9808	1.073	19.724	5.1
427	J140744.85+525211.5	211.9369	52.8699	1.073	20.273	5.4
428	J141856.19+535845.0	214.7341	53.9792	0.976	18.299	30.4	45.4	...	8.7
437	J141723.08+540641.5	214.3462	54.1115	0.856	19.791	12.0	44.7	...	8.3
438	J140733.13+531254.1	211.8880	53.2150	0.826	19.698	5.8	44.5	44.2	8.6
439	J141049.76+540040.6	212.7073	54.0113	0.834	21.126	3.2	44.0	44.0	7.8
440	J142209.14+530559.8	215.5381	53.0999	0.754	19.527	15.6	44.7	44.1	9.1
443	J141811.08+520618.0	214.5462	52.1050	1.122	20.923	4.3
450	J142217.19+530211.2	215.5716	53.0364	0.896	20.585	6.3	44.4	43.6	8.6
453	J141058.78+520712.2	212.7449	52.1200	0.391	20.001	4.2	43.6	43.3	8.4
457	J141417.13+515722.6	213.5714	51.9563	0.604	20.288	2.1	43.4	43.5	8.1
460	J141634.36+515849.3	214.1432	51.9804	0.990	19.293	15.8	45.0	...	8.9
465	J142008.27+521646.9	215.0345	52.2797	1.059	18.188	31.6

Table 1
(Continued)

RMID	SDSS Identifier	R.A. ^a	Decl. ^a	z^a	i mag ^a	MED ^b S/N	AGN	Host	log $M_{\text{BH,SE}}^c$ (M_{\odot})
		(deg) (J2000)	(deg) (J2000)				log $\lambda L_{\lambda 5100}^c$ (erg s ⁻¹)	log $\lambda L_{\lambda 5100}^c$ (erg s ⁻¹)	
469	J142106.27+534407.0	215.2761	53.7353	1.006	18.307	24.9	45.4	...	9.0
472	J141104.87+520516.8	212.7703	52.0880	1.080	18.982	19.1
478	J140726.47+524710.5	211.8603	52.7862	0.957	19.495	7.4	44.6	44.1	8.7
480	J140752.37+523622.3	211.9682	52.6062	0.996	21.361	1.7	44.2	44.6	8.2
489	J142120.78+534235.8	215.3366	53.7099	1.002	20.834	3.0	44.4	...	7.9
492	J141154.13+520023.4	212.9755	52.0065	0.963	18.953	17.4	45.0	43.6	8.7
497	J142236.11+530923.2	215.6505	53.1564	0.511	19.311	8.7	44.2	44.2	9.5
510	J140820.78+522444.3	212.0866	52.4123	0.710	20.780	4.1	44.1	43.7	8.3
515	J141808.04+520023.3	214.5335	52.0065	0.805	20.326	6.2	44.4	44.2	8.8
518	J142222.79+524354.0	215.5949	52.7317	0.459	20.069	4.0	43.9	...	7.3
519	J141712.30+515645.5	214.3012	51.9460	0.554	21.537	1.5	43.2	43.2	7.4
525	J140929.77+535930.0	212.3740	53.9917	0.863	19.666	11.9	44.7	...	7.6
539	J141816.11+541120.0	214.5671	54.1889	0.846	20.733	3.4	44.1	...	8.7
541	J141852.64+520142.8	214.7193	52.0286	0.440	20.590	4.7	43.5	43.3	7.7
545	J140643.27+531619.6	211.6803	53.2721	0.979	19.770	12.4	44.9	...	9.0
546	J141928.58+520439.4	214.8691	52.0776	1.028	21.368	2.9	44.6	44.6	8.1
548	J141553.09+541816.5	213.9712	54.3046	0.731	20.594	5.9	44.1	43.9	7.5
551	J141147.06+515619.8	212.9461	51.9388	0.680	21.522	5.3	44.0	43.7	7.7
572	J141809.85+515531.6	214.5411	51.9255	0.990	19.493	9.5	44.9	...	9.1
588	J142304.15+524630.2	215.7673	52.7750	0.998	18.642	24.8	45.3	43.4	8.5
589	J142049.28+521053.3	215.2053	52.1815	0.751	20.740	8.9	44.4	43.8	8.5
593	J141623.53+514912.7	214.0980	51.8202	0.990	19.836	8.9	44.7	...	8.1
601	J140904.43+540344.2	212.2685	54.0623	0.658	20.100	5.1	44.1	43.6	9.1
618	J141625.25+542312.4	214.1052	54.3868	0.755	21.432	2.1	43.6	43.9	7.7
622	J141115.19+515209.0	212.8133	51.8692	0.572	19.554	12.2	44.3	43.7	8.2
632	J141637.17+514627.1	214.1549	51.7742	0.681	21.587	1.6	43.6	43.3	8.2
634	J141135.89+515004.5	212.8995	51.8346	0.650	20.758	3.8	44.0	43.6	7.5
637	J142129.26+521153.3	215.3719	52.1981	0.848	19.046	13.8	44.8	...	7.8
638	J141753.58+514918.4	214.4732	51.8218	0.677	20.654	5.9	44.2	44.0	8.4
641	J141405.66+514425.9	213.5236	51.7405	0.805	21.223	3.1	44.0	44.0	8.6
643	J142119.53+520959.7	215.3314	52.1666	0.961	21.154	3.5	44.2	44.2	8.5
644	J142301.87+523316.7	215.7578	52.5546	0.845	20.205	6.0	44.5	...	8.8
645	J142039.80+520359.7	215.1658	52.0666	0.474	19.783	9.2	44.1	43.2	8.2
649	J140554.86+525347.5	211.4786	52.8965	0.849	20.485	4.7	44.3	44.1	8.0
653	J142346.35+531807.4	215.9431	53.3020	0.883	20.392	2.7	44.2	44.1	8.1
654	J142353.92+530722.7	215.9747	53.1230	0.670	20.937	3.6	43.8	43.8	8.2
659	J141528.40+514308.7	213.8683	51.7191	0.922	19.524	10.9	44.8	...	8.3
663	J142346.21+532212.5	215.9425	53.3701	0.674	20.479	4.3	44.0	43.5	8.1
664	J141202.26+514638.5	213.0094	51.7774	0.840	20.665	9.2	44.6	...	8.3
668	J140553.05+532448.1	211.4711	53.4134	0.853	20.408	3.3	44.3	44.1	8.3
669	J140548.18+525041.0	211.4507	52.8447	0.839	20.144	4.8	44.4	...	8.5
675	J140843.80+540751.3	212.1825	54.1309	0.918	19.462	12.3	44.8	...	8.8
681	J142235.20+522059.1	215.6466	52.3498	0.972	21.660	3.2	44.2	44.0	8.7
685	J142336.77+523932.8	215.9032	52.6591	0.962	19.871	9.4	45.0	44.0	8.5
694	J141706.68+514340.1	214.2778	51.7278	0.532	19.621	10.3	44.2	43.6	7.6
697	J141932.16+515228.6	214.8840	51.8746	1.028	21.223	2.9	44.6	44.5	7.9
701	J140715.49+535610.2	211.8145	53.9362	0.683	19.735	7.7	44.3	43.9	8.5
707	J142417.22+530208.9	216.0718	53.0358	0.890	21.154	2.9	44.1	43.9	7.6
714	J142349.72+523903.6	215.9572	52.6510	0.921	19.643	6.9	44.6	43.9	8.9
719	J141734.88+514237.8	214.3953	51.7105	0.800	21.662	2.6	43.8	43.6	7.9
720	J140518.02+531530.0	211.3251	53.2583	0.467	19.030	13.7	44.3	43.4	8.1
728	J142419.55+531859.9	216.0815	53.3167	1.129	21.550	3.3
733	J140551.99+533852.1	211.4666	53.6478	0.455	19.904	6.7	43.9	43.4	8.2
736	J140508.60+530539.0	211.2858	53.0942	0.582	18.248	20.9	44.7	...	8.6
744	J141615.83+543126.4	214.0659	54.5240	0.723	21.361	1.7	43.4	43.9	7.6
746	J141720.29+514032.4	214.3345	51.6757	0.683	19.703	13.2	44.5	44.0	8.1
750	J140522.76+524301.7	211.3448	52.7171	0.950	20.937	3.5	44.4	44.0	8.3
756	J140923.42+515120.1	212.3476	51.8556	0.853	20.292	4.2	44.1	44.1	8.2
757	J141902.09+514459.1	214.7587	51.7498	1.125	21.072	3.1
761	J142412.93+523903.4	216.0539	52.6510	0.771	20.426	9.6	44.5	...	8.5
762	J141919.08+542432.8	214.8295	54.4091	0.782	20.475	8.2	44.6	...	8.9
764	J142222.21+520819.3	215.5925	52.1387	0.985	20.900	2.0	43.8	44.3	8.1

Table 1
(Continued)

RMID	SDSS Identifier	R.A. ^a	Decl. ^a	z^a	i mag ^a	MED ^b S/N	AGN	Host	log $M_{\text{BH,SE}}^c$ (M_{\odot})
		(deg) (J2000)	(deg) (J2000)				log $\lambda L_{\lambda 5100}^c$ (erg s ⁻¹)	log $\lambda L_{\lambda 5100}^c$ (erg s ⁻¹)	
766	J141419.84+533815.3	213.5827	53.6376	0.165	17.461	41.3	43.7	43.6	7.5
767	J141650.93+535157.0	214.2122	53.8658	0.527	20.233	4.1	43.9	...	7.5
768	J140915.70+532721.8	212.3154	53.4561	0.258	18.875	17.8	43.3	43.7	8.7
769	J141253.92+540014.4	213.2247	54.0040	0.187	18.702	16.7	43.0	43.4	7.9
772	J142135.90+523138.9	215.3996	52.5275	0.249	18.870	14.8	43.4	43.6	7.6
773	J141701.93+541340.5	214.2581	54.2279	1.103	19.262	13.1
775	J140759.07+534759.8	211.9961	53.7999	0.172	17.910	28.6	43.5	43.4	7.9
776	J140812.09+535303.3	212.0504	53.8842	0.116	17.976	25.7	43.1	43.0	7.8
778	J141418.55+542521.8	213.5773	54.4227	0.786	19.492	15.0	44.8	...	8.6
779	J141923.37+542201.7	214.8474	54.3671	0.152	19.096	11.9	43.1	42.6	7.4
781	J142103.53+515819.5	215.2647	51.9721	0.263	19.305	14.7	43.6	43.3	7.8
782	J141318.96+543202.4	213.3290	54.5340	0.362	18.892	13.9	43.9	43.6	8.0
783	J141319.83+513718.1	213.3326	51.6217	0.984	18.797	20.3	45.1	...	8.5
788	J141231.73+525837.9	213.1322	52.9772	0.843	21.232	1.7	43.8	44.1	8.4
789	J141644.17+532556.1	214.1840	53.4322	0.425	20.203	7.6	43.7	43.3	8.1
790	J141729.27+531826.5	214.3720	53.3074	0.237	18.672	19.5	43.3	43.6	8.4
792	J141800.72+532035.9	214.5030	53.3433	0.526	20.636	3.1	43.0	43.8	7.8
797	J141427.89+535309.7	213.6162	53.8860	0.242	19.997	8.2	43.1	43.0	7.0
798	J141202.88+522026.1	213.0120	52.3406	0.423	19.145	15.8	44.0	43.7	7.6
804	J142100.04+532139.6	215.2502	53.3610	0.677	20.347	6.2	44.0	43.9	7.5
805	J140827.04+532323.3	212.1127	53.3898	0.620	20.328	6.3	44.0	43.4	7.8
808	J141546.21+540954.7	213.9425	54.1652	0.956	20.111	6.6	44.6	44.0	9.0
812	J141945.51+521342.2	214.9396	52.2284	0.702	20.181	5.7	44.0	44.1	8.4
813	J141222.07+541020.0	213.0919	54.1722	0.955	20.759	4.5	44.3	43.8	7.5
814	J140741.04+524037.0	211.9210	52.6769	0.958	21.269	2.7	44.3	44.0	8.7
822	J141308.10+515210.4	213.2838	51.8695	0.288	19.182	13.3	43.6	43.5	7.4
823	J141501.64+541930.9	213.7568	54.3253	1.101	21.069	2.8
824	J141038.11+520032.9	212.6588	52.0091	0.845	21.526	2.7	43.9	43.8	8.5
838	J141731.16+542350.4	214.3799	54.3973	0.855	21.212	1.9	43.9	44.1	8.5
839	J141358.91+542706.0	213.4954	54.4517	0.975	20.644	2.2	44.2	44.1	9.1
840	J141645.15+542540.8	214.1881	54.4280	0.244	18.632	14.1	43.2	43.5	8.3
843	J141907.91+530025.5	214.7830	53.0071	0.563	20.846	2.8	43.3	43.7	7.6
845	J142321.70+532242.7	215.8404	53.3785	0.273	19.665	6.9	42.7	43.5	7.7
846	J142241.37+532646.7	215.6724	53.4463	0.228	21.540	1.3	41.8	42.4	7.5
847	J142324.24+533511.2	215.8510	53.5864	0.758	19.965	5.9	44.3	44.4	9.0
848	J142225.62+533426.3	215.6067	53.5740	0.757	20.806	3.3	43.7	44.2	7.8

Notes.

^a These measurements were made as a part of the SDSS Data Release 10 (Ahn et al. 2014). The i magnitudes listed are point-spread function magnitudes and have not been corrected for Galactic extinction.

^b MED-S/N, where S/N is the median signal-to-noise ratio per SDSS pixel across each individual spectrum, and MED-S/N is the median across all epochs (each SDSS pixel spans 69 km s⁻¹).

^c These measurements are taken from Shen et al. (2015b). The $M_{\text{BH,SE}}$ estimates were made using the Vestergaard & Peterson (2006) prescription for L_{5100} .

(This table is available in its entirety in machine-readable form.)

2.2. Spectroscopic Data

The SDSS-RM spectroscopic data utilized in this work were all acquired with the BOSS spectrograph between 2014 January and July. The BOSS spectrograph covers a wavelength range of $\sim 3650\text{--}10400 \text{ \AA}$ and has a spectral resolution of $R \sim 2000$. The processed spectra are binned to 69 km s⁻¹ pixel⁻¹. We obtained a total of 32 spectroscopic epochs with a median of 4.0 days between observations and a maximum separation of 16.6 days. The observations were scheduled during dark time and occasionally had interruptions due to weather or scheduling constraints, so the cadence of the observations varies somewhat throughout the season. Figure 2 shows the actual observing cadence. The typical exposure time was 2 hr. The data were processed by the SDSS-III pipeline and then further processed using a custom flux-calibration scheme

described in detail by Shen et al. (2015a). We measure the median S/N per pixel in each epoch for each source, and we take the median among all epochs as our measure of the overall S/N for each source, which we designate as SN-MED. The distribution of SN-MED for our sample is shown in Figure 1.

To improve our relative flux calibrations and produce light curves, we employ a series of custom procedures as implemented in a code called PrepSpec, which is described in detail by Shen et al. (2016b, 2015a). A key feature of PrepSpec is the inclusion of a time-dependent flux correction calculated by assuming that there is no intrinsic variability of the narrow emission-line fluxes over the course of the RM campaign. PrepSpec minimizes the apparent variability of the narrow lines by fitting a model to the spectra that includes intrinsic variations in both the continuum and broad emission

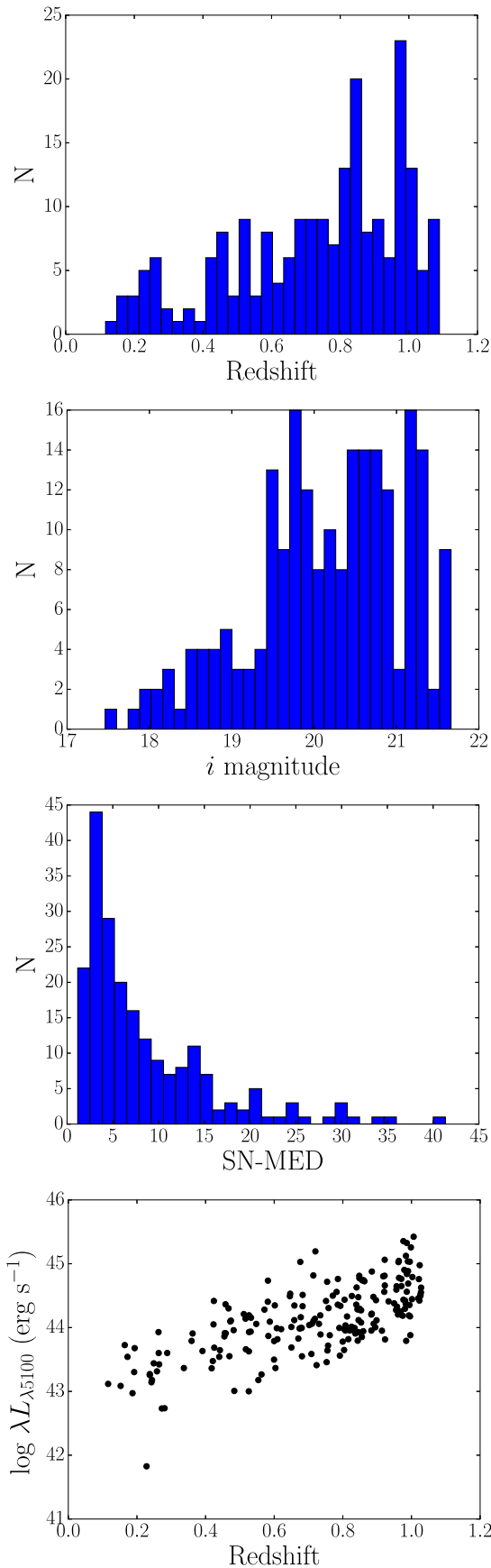


Figure 1. From top to bottom: the distributions of our sample of quasars in redshift, i magnitude, median SN-MED (see Section 2.1), and $\lambda L_{\lambda 5100}$ (the host-subtracted quasar continuum luminosity at 5100 Å) as a function of redshift.

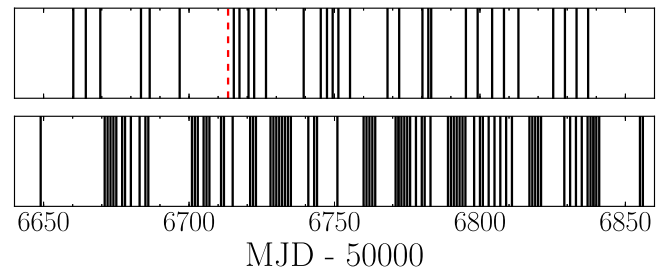


Figure 2. Observing cadence for the spectroscopic observations (top panel) and photometric observations (bottom panel). Each vertical black line represents an observed epoch. The seventh spectroscopic epoch, shown as a red dashed line, has much lower S/N and is frequently an outlier in the light curves, so it is excluded from our analysis.

lines. PrepSpec is similar to recent spectral decomposition approaches (e.g., Barth et al. 2015), but it is optimized to fit all of the spectra of an object simultaneously and includes this flux-calibration correction. The PrepSpec model also incorporates components to account for variations in seeing and small wavelength shifts. PrepSpec produces measurements of line fluxes, mean and root mean square (rms) residual line profiles, line widths, and light curves for each of the model components. We note that the PrepSpec rms line profiles do not include the continuum and thus differ from commonly measured rms line profiles that often still include the continuum (see Section 4.2 for details).

We compute g - and i -band synthetic photometry from each PrepSpec-scaled spectrum by convolving it with the corresponding SDSS filter response curves (Fukugita et al. 1996; Doi et al. 2010). We estimate uncertainties in the synthetic photometric fluxes as the quadratic-sum uncertainties resulting from the measurement errors in the spectrum and errors in the flux-correction factor from PrepSpec. We then later merge these light curves with the photometric light curves to improve the cadence of the continuum light curves (see Section 2.4 below). We calculate emission-line light curves directly from the PrepSpec fits.

Of the 32 available epochs, two (the third and seventh epochs) were acquired under poor observing conditions, resulting in spectra with significantly lower S/Ns than the other epochs. Upon inspection, the seventh epoch (MJD 56713) appeared as a significant outlier in a large fraction of the light curves (more than 33% of the $H\beta$ light curves). We therefore removed Epoch 7 from all of our spectroscopic light curves. There were also occasional cases of “dropped” epochs or loose fibers; these are cases where the fibers were not plugged correctly or the SDSS pipeline failed to extract a spectrum for various reasons. Loose fibers appear as significant low-flux outliers in the light curves, while dropped epochs appear as epochs with zero flux. We excluded all epochs with zero flux and epochs with loose fibers by rejecting points that were offset from the median flux by more than 5 times the normalized median absolute deviation (NMAD; e.g., Maronna et al. 2006) of the light curve (this threshold was established by visual inspection; see also Sun et al. 2015 for a discussion of dropped fibers). The final emission-line light curves of all 222 quasars are given in Table 2. We include all spectroscopic epochs in the table and mark those that were excluded from our analysis with a rejection flag (FLAG = 1).

Table 2
RM 005 Light Curves

MJD (-50000)	Band ^a	Telescope ^b	Flux ^c	Error ^c	FLAG ^d
6660.2090	<i>g</i>	S	16.99	0.33	0
6664.5130	<i>g</i>	S	16.99	0.33	0
6669.5003	<i>g</i>	S	16.90	0.34	0
6686.4734	<i>g</i>	S	17.47	0.35	0
6711.5226	<i>g</i>	C	17.48	0.19	0
6712.4684	<i>g</i>	C	17.75	0.18	0
6712.4694	<i>g</i>	C	17.28	0.18	0
6712.4703	<i>g</i>	C	17.48	0.19	0
6715.4106	<i>g</i>	C	17.37	0.20	0
6715.4116	<i>g</i>	C	17.43	0.20	0
6715.4125	<i>g</i>	C	17.40	0.19	0
6715.5388	<i>g</i>	C	17.15	0.18	0
6715.5397	<i>g</i>	C	17.50	0.18	0
6715.5407	<i>g</i>	C	16.95	0.18	0
6715.5416	<i>g</i>	C	17.31	0.19	0
6717.3345	<i>g</i>	S	17.15	0.34	0
6720.4456	<i>g</i>	S	17.08	0.34	0

Notes. Light curves for all 222 quasars can be found online. A portion is shown here for guidance in formatting.

^a $H\beta = H\beta$ emission line, $H\alpha = H\alpha$ emission line, $g = g$ band, and $i = i$ band.

^b C = CFHT, B = Bok, S = SDSS.

^c Continuum flux densities and uncertainties are in units of 10^{-17} erg s^{-1} cm^{-2} \AA^{-1} . Integrated emission-line fluxes are in units of 10^{-17} erg s^{-1} cm^{-2} . The fluxes are not host-subtracted.

^d Emission-line epochs with FLAG = 1 were identified as outliers and excluded from the light curves in our analysis.

(This table is available in its entirety in machine-readable form.)

2.3. Photometric Data

In addition to spectroscopic monitoring with SDSS, we have been observing the SDSS-RM quasars in both the g and i bands with the Steward Observatory Bok 2.3 m telescope on Kitt Peak and the 3.6 m Canada–France–Hawaii Telescope on Maunakea. Details of the photometric observations and the subsequent data processing will be presented by K. Kinemuchi et al. (2017, in preparation). The Bok/90Prime instrument (Williams et al. 2004) used for our observations has a $\sim 1^\circ \times 1^\circ$ field of view using four $4k \times 4k$ CCDs each with a plate scale of $0''.45$ pixel $^{-1}$. Over 60 nights between 2014 January and June, largely during bright time, we obtained 31 epochs in the g band and 27 epochs in i . The CFHT MegaCam instrument (Aune et al. 2003) also has a $\sim 1^\circ \times 1^\circ$ field of view, but has a pixel size of $0''.187$. Over the 2014 observing period, we obtained 26 epochs in g and 20 in i , with a few additional epochs in each band where only some of the fields were observed.

To produce photometric light curves, we adopt image subtraction as implemented in the software package ISIS (Alard & Lupton 1998; Alard 2000). The basic procedure is to first align the images and create a reference image by combining the best images (seeing, transparency, sky background). ISIS then alters the point-spread function (PSF) of the reference image and scales the target image in overall flux calibration. It then subtracts the two to leave a “difference” image with the same flux calibration as the reference image, showing the sources that have changed in flux. We then place a PSF-weighted aperture over each source and measure the

residual flux in each of the subtracted images to produce light curves. We separately produced reference images and performed the subtraction for each individual telescope, filter, CCD, and field.

After the image subtraction was complete, we removed bad measurements or outliers from the photometric light curves; these include points for sources that have fallen off the edge of the detector in certain epochs, saturated sources (either bright quasars themselves or those near a bright star, which show a large dispersion in flux in the differential photometry), and images affected by passing cirrus or other problems that deviate from the median by >5 times the NMAD of the light curve.

While the image-subtraction technique allows one to better compensate for changes in seeing and to separate seeing-dependent aperture effects from real variability, the ISIS software takes into account only local Poisson error contributions. There are also systematic uncertainties that are not well captured by these estimates. We follow the procedure outlined by Hartman et al. (2004) and Fausnaugh et al. (2016, 2017) to apply corrections to the ISIS uncertainties. We extracted light curves for stars of magnitude similar to that of the quasars, most of which should be nonvariable. After eliminating the few variable stars, we determine an error-rescaling factor necessary for each standard star light curve to be consistent with a constant-flux model and plot this factor as a function of magnitude for each CCD/field combination. This provides an estimated error-rescaling factor as a function of magnitude, which we fit as a polynomial and multiply the error estimates by. Scale factors were typically about a factor of two, but range from ~ 1 for fainter sources to ~ 10 for the brightest sources. We did not apply scale factors less than 1 (i.e., we did not reduce any uncertainties from their ISIS-reported values).

2.4. Light Curve Intercalibration

We have several individual photometric light curves (one for each telescope/field/CCD observation) and a single synthetic photometric light curve (produced from the spectra) in each band for each quasar. For our analysis, it is necessary to place all of the g - and i -band light curves from all CCDs/telescopes/fields on the same flux scale; this intercalibration accounts for different detector properties, different telescope throughputs, and other properties specific to the individual telescopes involved. We assume that the time lag between the g and i band is much smaller than we are able to resolve with our data and thus can be treated as zero for intercalibration purposes.

We performed this intercalibration using the Continuum REprocessing AGN MCMC (CREAM) software recently developed by Starkey et al. (2016). CREAM uses Markov chain Monte Carlo (MCMC) techniques to model the light curves, assuming that the continuum emission is emitted from a central location and is reprocessed by more distant gas (see Starkey et al. 2016 for a thorough discussion of the technique). CREAM fits a model driving light curve $X(t)$ to the g - and i -band light curves $f_j(\lambda, t)$ with an accretion-disk response function $\psi(\tau|\lambda)$. The model is

$$f_j(\lambda, t) = \bar{F}_j(\lambda) + \Delta F_j(\lambda) \int_0^\infty \psi(\tau|\lambda) X(t - \tau) d\tau, \quad (2)$$

where each telescope j is assigned an offset $\bar{F}_j(\lambda)$ and flux scaling parameter $\Delta F_j(\lambda)$. The offset and scaling parameters control the intercalibration of the g or i light curves, from multiple telescopes, onto the same scale.

These parameters are optimized in the MCMC fit, and the rescaled g and i light curves are calculated from the original light curves using

$$f_{j,\text{new}}(\lambda, t) = (f_{j,\text{old}}(\lambda, t) - \bar{F}_j) \frac{\Delta F_{\text{REF}}}{\Delta F_j} + \bar{F}_{\text{REF}}, \quad (3)$$

where the subscript REF indicates the reference telescope/filter combination, and j is calculated for all telescopes at each g or i wavelength. CREAM was initially designed to calculate interband continuum lags by fitting the accretion-disk response function $\psi(\tau|\lambda)$. This function is not required in the merging process here—we are only interested in the intercalibration parameters $\bar{F}_j(\lambda)$ and $\Delta F_j(\lambda)$. We therefore alter CREAM such that it has a delta function response at zero lag $\psi(\tau|\lambda) = \delta(\tau - 0)$ for the continuum light curves in each g and i filter.

CREAM’s MCMC algorithm also rescales the nominal error bars using an extra variance, V_j , and scale factor parameters, f_j , for each telescope (Starkey et al. 2017). The rescaled error bars are

$$\sigma_{ij} = \sqrt{(f_j \sigma_{\text{old}, ij})^2 + V_j}, \quad (4)$$

where $i = 1 \dots N_j$ is an index running over the N_j data points for telescope j . The likelihood function L_j penalizes high values of V_j and f_j in the MCMC chain and is given by

$$-2 \ln L_j = N_j \ln(2\pi) + \sum_{i=1}^{N_j} \left[\ln \sigma_{ij}^2 + \left(\frac{D_{ij} - M_{ij}}{\sigma_{ij}} \right)^2 \right], \quad (5)$$

for data D_{ij} and model M_{ij} . This approach provides an additional check or correction on the uncertainties for our continuum light curves.

The resulting improved “merged” light curves from CREAM are used in our RM time-series analysis. Figure 3 presents an example set of light curves for SDSS J141625.71+535438.5. The final, intercalibrated light curves for the 222 quasars are provided in Table 2.

3. Time-series Analysis

3.1. Lag Measurements

Most prior RM measurements have been based upon cross-correlation methods and simple linear interpolation between observations (e.g., Peterson et al. 2004). However, over the past several years, more sophisticated procedures have been developed that model the statistically likely behavior of the light curves in the gaps between observations (e.g., JAVELIN, Zu et al. 2011; and CREAM, Starkey et al. 2016). These procedures provide three key improvements over linear interpolation. Most importantly, their light curves have higher uncertainties in the interpolated regions compared to the observed light curve points, in contrast to the smaller uncertainties between points when using simple linear interpolation. JAVELIN and CREAM also use a damped random walk (DRW) model for the variability, matching observations (e.g., Kelly et al. 2009; Kozłowski et al. 2010; MacLeod et al. 2010). Finally, they use the same continuum DRW model fit, with a transfer function, to describe the broad-line light curves. This is essentially a prior that the BLR reverberates (although it allows either a positive or negative reverberation delay). This

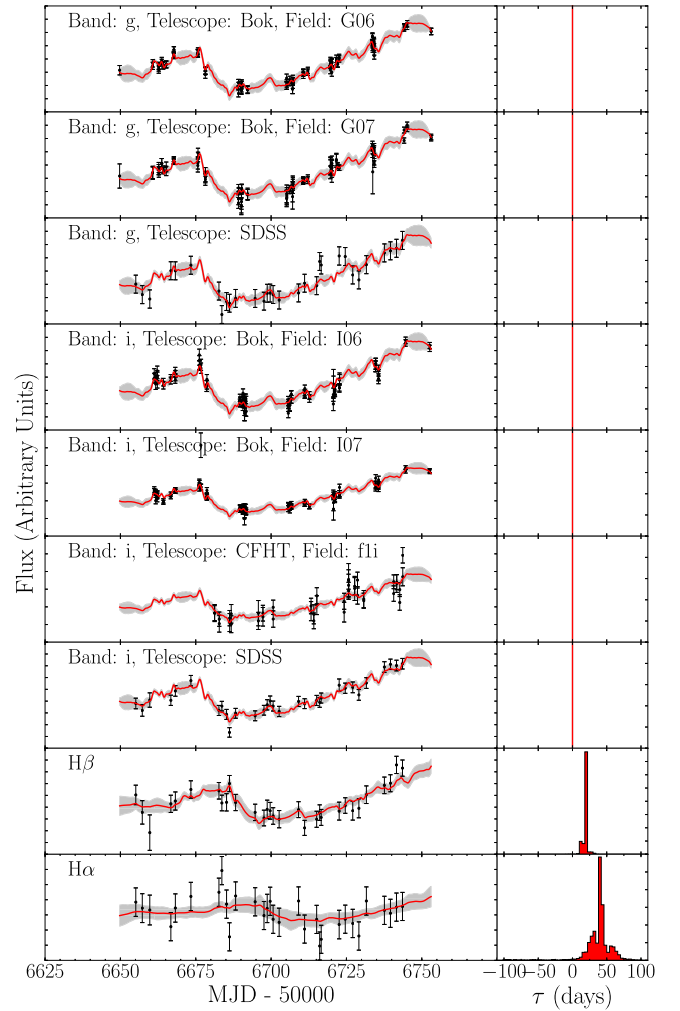


Figure 3. CREAM model fits to the light curves for SDSS J141625.71+535438.5 (RMID 272, $z = 0.263$) as a demonstration of the intercalibration technique. Each left panel shows an individual premerged light curve (black points) with the CREAM model fit and uncertainties in red and gray, respectively. The right panels display the corresponding CREAM-calculated posterior distribution of observed-frame time lags calculated for each light curve’s response function $\psi(\tau)$. The time lag between the photometric light curves and the synthetic spectroscopic light curves is fixed to zero in order to intercalibrate the data.

assumption is the basic reason that reverberation mapping is possible, although recent observations have also identified periods of nonreverberating variability in NGC 5548 (Goad et al. 2016).

We performed our time-series analysis using all three of these methods, with the goal of comparing and contrasting the results from simple interpolation/cross-correlation and different prescriptions for statistical modeling of light curves. All of our time-series analysis is performed in the observed frame, and measured time delays are later shifted into the rest frame. Because our light curves span only about 200 days, we restrict our search to lags from -100 to $+100$ days. For larger and smaller lags, the overlap between the two light curves is reduced to less than half, making it harder to judge the validity of identifying correlated features. Future data spanning multiple years will soon be able to provide more reliable estimates for longer lags.

The most common methods to measure RM time lags are the interpolated cross-correlation function (ICCF; e.g., Gaskell &

Peterson 1987; Peterson et al. 2004) and the discrete correlation function (DCF; Edelson & Krolik 1988) or z -transformed DCF (zDCF; Alexander 1997). The DCF has been shown to perform best when large numbers of points are present; for cases with lower sampling such as our data, it is better to use the ICCF (White & Peterson 1994). The zDCF was designed to mitigate some of the issues with the DCF; however, for this study we opted to use the ICCF, as it is more traditionally used, and a detailed comparison between the ICCF and zDCF is not yet available in the literature. The ICCF method works as follows: for a given time delay τ , we shift the time coordinates of the first light curve by τ and then linearly interpolate the second light curve to the new time coordinates, measuring the cross-correlation Pearson coefficient r between the two light curves using overlapping points. We next shift the second light curve by $-\tau$ and interpolate the first light curve, and average the two values of r . This process is repeated over the entire range of allowed τ , evaluating r at discrete steps in τ . This procedure allows the measurement of r as a function of τ , called the ICCF. The centroid (τ_{cent}) of the ICCF is measured using points surrounding the maximum correlation coefficient r_{max} out to $r \geq 0.8r_{\text{max}}$, as is standard for ICCF analysis (e.g., Peterson et al. 2004).

We calculated ICCFs and τ_{cent} for our entire sample of quasars using an interpolation grid spacing of 2 days, calculating the ICCF between -100 and 100 days. Following Peterson et al. (2004), we estimate the uncertainty in τ_{ICCF} using Monte Carlo simulations that employ the flux randomization/random subset sampling (FR/RSS) method. Each Monte Carlo realization randomly selects a subset of the data and alters the flux of each point on the light curves by a random Gaussian deviate scaled to the measurement uncertainty of that particular point. We then calculate the ICCF for the altered set of light curves and measure τ_{cent} and τ_{peak} . This procedure is repeated 5000 times to obtain the cross-correlation centroid distribution (CCCD), and the uncertainties are determined from this distribution. We adopt the median of the distribution as the best τ_{ICCF} measurement after some modifications and the removal of aliases (described below in Section 3.2). Many previous studies adopted the centroid as measured from the actual ICCF rather than the median from the CCCD. However, we use the median of the CCCD because in the case of light curves with lower time sampling, the ICCF centroid can often be an outlier in the CCCD, suggesting that the median of the CCCD is a better characterization of the true lag. However, we do note that for our data, results using the centroid of the ICCF are nearly identical to measurements using the median of the CCCD.

We used the modeling code JAVELIN (Zu et al. 2011, 2013) as our primary time-series analysis method. Rather than linearly interpolating between light curve points, JAVELIN models the light curves as an autoregressive process using a DRW model and treats the emission-line light curves as scaled, shifted, and smoothed versions of the continuum light curves. The DRW model is observed to be a good description of quasar variability within the time regime relevant to our study (e.g., Kelly et al. 2009; Kozłowski et al. 2010, 2016; MacLeod et al. 2010, 2012), so it is an effective prior to describe the light curve between observations. JAVELIN builds a model of both light curves and simultaneously fits a transfer function, maximizing the likelihood of the model and computing uncertainties using the (Bayesian) Markov chain Monte Carlo

technique. The advantage of a method such as JAVELIN over the ICCF is that it replaces linear interpolation with a statistically and observationally motivated model of how to interpolate in time. The JAVELIN lag measurement takes into account the (increased) uncertainty associated with the interpolation between data points while including the statistically likely behavior of the intrinsic light curve. When multiple light curves of different emission lines are available, JAVELIN can model them simultaneously, which improves its performance and helps to eliminate multiple solutions.

The time span of our campaign observations (~ 190 days) is shorter than the typical damping timescale of a quasar (~ 200 – 1000 days; Kelly et al. 2009; MacLeod et al. 2012; Sun et al. 2015), so JAVELIN is unable to constrain this quantity with our data (e.g., Kozłowski 2017). We thus fix the JAVELIN DRW damping timescale to be 300 days (the exact choice of timescale does not matter as long as it is longer than the baseline of our data). We use a top-hat transfer function that is parameterized by a scaling factor, width, and time delay (which we denote as τ_{JAV}) with the width fixed to 2.0 days and the time delay restricted to be within -100 to 100 days. The best-fit lag and its uncertainties are calculated from the posterior lag distribution from the MCMC chain.

As discussed in Section 2.4, Starkey et al. (2016) recently developed an alternate approach to modeling light curves and measuring time delays called CREAM. In addition to merging the g and i light curves, CREAM is also able to infer simultaneously the $H\alpha$ and $H\beta$ lags. To achieve this, we assign a delta function response to the $H\alpha$ and $H\beta$ lags such that $\psi(\tau|\lambda) = \delta(\tau - \tau_{\text{BLR}})$, where τ_{BLR} is a fitted parameter in the MCMC chain along with the intercalibration parameters $\bar{F}_j(\lambda)$ and $\Delta F_j(\lambda)$ (see Equation (2)). CREAM self-consistently accounts for the joint errors in calibration and merging of the light curves when determining the lag. The CREAM posterior probability histograms for the τ_{BLR} parameters are shown for an example source in Figure 3. We again measure the best-fit lag (here denoted τ_{CREAM}) from the posterior lag distribution for the corresponding emission line.

All RM methods operate under the assumption that the broad-line region responds to a “driving” continuum light curve; this assumption is generally well justified given that most monitored AGNs have been observed to reverberate. However, there is a question as to whether or not the 5100 \AA continuum emission is a good proxy for the actual emission driving the emission-line response. We discuss this possible issue in Section 4.3.

3.2. Alias Identification and Removal

Examinations of the CCCD or posterior lag distributions from JAVELIN or CREAM frequently reveal a clear high-significance peak in the distribution accompanied by additional lower-significance peaks. In general, the presence of multiple peaks or a broad distribution of lags can indicate that the lag is not well constrained. In some cases, however, one peak is clearly strongest, and the additional weaker peaks are simply aliases resulting from the limited cadence and duration of the light curves. Aliases can sometimes be comparable in strength to the correct time lag, and they often appear in light curves with multiple peaks or troughs. These aliases can skew the τ measurements or produce uncertainties that are extremely large. It is therefore necessary to identify and remove aliases or

additional secondary peaks to obtain the best lag measurement and associated uncertainty.

Multiple CCCD peaks have been a common feature of previous RM observations, but alias removal in these single-object campaigns was typically applied by visual inspection in an ad hoc way (B. Peterson 2017, private communication). We instead developed a quantitative technique for alias rejection, appropriate for multiobject RM surveys like SDSS-RM. First, we applied a weight on the distribution of τ measurements in the posterior probability distributions that takes into account the number of overlapping spectral epochs at each time delay. If the true lag is so large that shifting by τ leaves no overlap between the two light curves, then we have a prior expectation that the true lag τ is not detectable with these data. If shifting one light curve by τ leaves $N(\tau)$ data points in the overlap region, we may expect to be able to detect τ with a prior probability that is an increasing function of $N(\tau)$. We define this weight $P(\tau) = [N(\tau)/N(0)]^2$, where $N(0)$ is the number of overlapping points at a time delay of zero. The weight on each τ measurement is thus 1 for $\tau = 0$ and decreases each time a data point moves outside the data overlap region when the light curve is shifted, eventually reaching zero when there is no overlap. Lags with few overlapping points are less likely to be reliable, since at fixed correlation coefficient r a smaller number of points leads to a higher null-probability p . In this way, the $N(\tau)$ prior acts as a conservative check on longer lags, requiring stronger evidence to conclude detections with less light curve overlap. We tested different exponents for $P(\tau) = (N(\tau)/N(0))^k$ and ultimately adopted $k = 2$ based on visual inspection of the apparent lags in the light curves. Figure 4 shows an example of the effect that this weighting has on the posterior lag distributions.

To identify peaks and aliases in the posterior distribution, we smoothed the posterior lag distributions (the cross-correlation CCCD or the JAVELIN/CREAM MCMC posterior lag distributions) by a Gaussian kernel with a width of 5 days (the choice of 5 days was determined by visual inspection). The tallest peak of the smoothed distribution was then identified as the primary lag peak. We searched for local minima on either side of this primary peak and rejected all lag samples that fell outside of these local minima. The lag τ and its uncertainties were then measured as the median and normalized mean absolute deviation of the remaining lag distribution. We performed this alias-removal procedure on the JAVELIN and CREAM posteriors and the ICCF CCCDs. Figure 4 provides a demonstration of this procedure. We note that the weighting discussed above is only used to select primary peaks and their accompanying lag samples (i.e., identify the range of lags to include); we make our lag measurements from the unweighted posteriors that fall within that lag range.

3.3. Lag-significance Criteria

In many cases, we find no significant correlation between the two light curves or are otherwise unable to obtain a good measurement of τ (i.e., the lag is formally consistent with zero when the uncertainties are taken into account). In order to consider the lag a “significant” detection, we require the following.

1. The measured τ is formally inconsistent with zero to at least 2σ significance (i.e., the absolute value of the lag is greater than twice its lower-bound uncertainty for

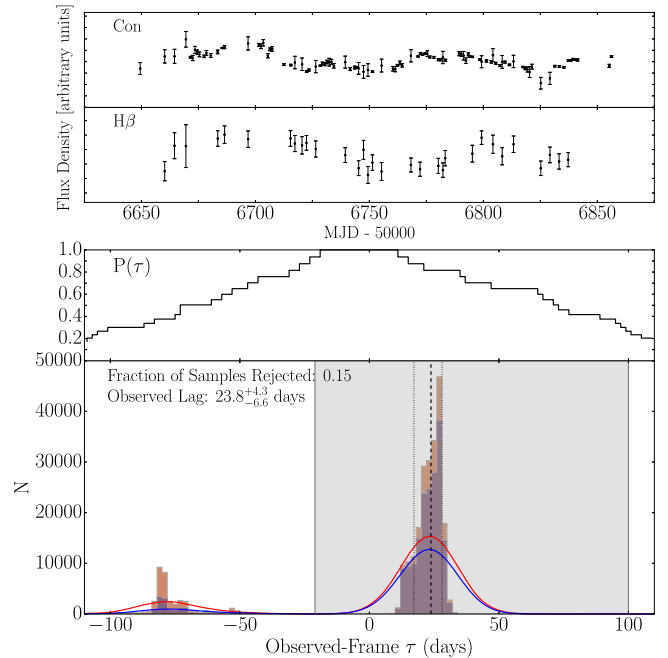


Figure 4. Light curves and the JAVELIN posterior $H\beta$ lag distribution for SDSS J141018.04+532937.5 (RMID 229, $z = 0.470$). The top two panels show the continuum and $H\beta$ light curve. For display purposes, multiple observations within a single night are averaged and shown as a single point. The third panel from the top shows $P(\tau)$ used to weight the posterior lag distribution. The pink shaded histogram shows the JAVELIN posterior lag distribution before applying the weights, and the purple shaded histogram is the posterior weighted by $P(\tau)$; see Section 3.2. The solid red and blue lines are the smoothed posterior distributions for the unweighted and weighted distributions, respectively. The gray shaded region shows the lag samples surrounding the main peak of the model distribution that were included in the final lag measurement for this source. Vertical black dashed and dotted lines indicate the measured time delay and its uncertainties, respectively, estimated from the median and the mean absolute deviation of the lag distribution within the shaded region.

positive lags and twice its upper-bound uncertainty for negative lags).

2. Less than half of the samples have been rejected during the alias-identification steps described above; if this alias-removal system excludes more than half of the samples, this is an indication that we lack a solid measurement of τ .
3. The maximum ICCF correlation coefficient, r_{\max} , must be greater than 0.45. This ensures that the behavior in the two light curves is well correlated. This number was determined to remove low-quality lag measurements and retain our highest-quality detections, as determined based on visual inspections of the light curves and the posterior distributions (see Section 3.5 for details).
4. The continuum and line light curve rms variability S/N is greater than 7.5 and 0.5, respectively (see below). This constraint excludes lag measurements that are due to spurious correlations between noisy light curves or long, monotonic trends rather than an actual reverberation signal, and it effectively requires that there is significant short-term variability in the light curves.

This final criterion requires measurements of the continuum and line light curve variance. To parameterize this, we define the “light curve S/N” as the intrinsic variance of the light curve about a fitted linear trend, divided by its uncertainty. First, a linear trend is fit to the light curves. Following Almaini et al.

(2000) and Sun et al. (2015), we measure the intrinsic variance from the observed g -band light curves using a maximum-likelihood estimator to account for the measurement uncertainties. The rms variation that we observe in the light curves, σ_{obs} , is a combination of the intrinsic variance σ_{int} and the measurement error σ_{err} , such that $\sigma_{\text{obs}}^2 = \sigma_{\text{int}}^2 + \sigma_{\text{err}}^2$. The maximum-likelihood estimator finds the intrinsic variance that maximizes the likelihood of reproducing the observed variance given the time-dependent error. Sources with short-term variability (i.e., variability other than a smooth trend) will show an excess variance about the fitted linear model, and it is only for these sources that reliable lags can be obtained.

As with our r_{max} threshold, our chosen light curve S/N thresholds were chosen to remove spurious lag measurements while still retaining all of our highest-quality lag detections. We note, however, that the light curve S/N as measured here is a somewhat coarse measure of the light curve quality for the purpose of lag determination, since it is a measure of the average variability over the entire light curve rather than a measure of short-term variations suitable for a lag measurement. This is why we require a line rms variability of only 0.5, since many $0.5 < \text{S/N} < 1$ light curves still contain significant short-term variations and a reverberation signal that meets our other criteria. Despite this, the light curve S/N remains a useful way to flag spurious correlations between noisy light curves or long, monotonic variability.

In order to estimate the false-positive detection rate of each method, we follow Shen et al. (2016b) and investigate the relative incidence of positive and negative lags. If all lag measurements were due to noise and not due to physical processes, one would expect to find equal numbers of positive and negative lags (we assume that there is no physical reason to measure a negative lag, and thus all negative lags are due to the noise or sampling properties of our light curves). Figure 5 shows the measured $H\beta$ τ_{JAV} for all 222 quasars as a function of our various detection threshold parameters. We find that there is a preference for both the detected and nondetected lag measurements to be positive, suggesting that, overall, we are measuring more physical lags. We also find that light curves with high intrinsic variability are more likely to show positive-lag detections, and there is a strong preference for “significant” $H\beta$ lags to be positive, which suggests that, statistically, we are detecting mostly real lag signals.

Of our significant $H\beta$ lag detections from JAVELIN, 32 are positive and 2 are negative; these negative lags can be considered “false positives,” as they are unphysical from an RM standpoint. Statistically speaking, this suggests that we likely have a similar number of “false positive” positive $H\beta$ lags as well, which is a $6.3_{-2.1}^{+7.3}\%$ false-positive rate (calculations of uncertainties follow Cameron 2011). We thus expect on the order of 30 of our $H\beta$ lag measurements from JAVELIN to be real. We observe a similar fraction of false positives in our $H\alpha$ lag measurements (not pictured), with 13 significant positive lags and one significant negative lag, corresponding to a false-positive rate of $7.7_{-2.6}^{+14.0}\%$. Shen et al. (2015a) simulated the expected quality of data from the SDSS-RM program (light curve cadence, S/N, and so on) and estimated a false-positive rate of between 10% and 20%, which is consistent with these estimates. Our criteria for reporting detected lags are quite stringent and are meant to be conservative: the overall preference for positive lags (both significant and insignificant) suggests that it is likely that we have “detected” lags in other

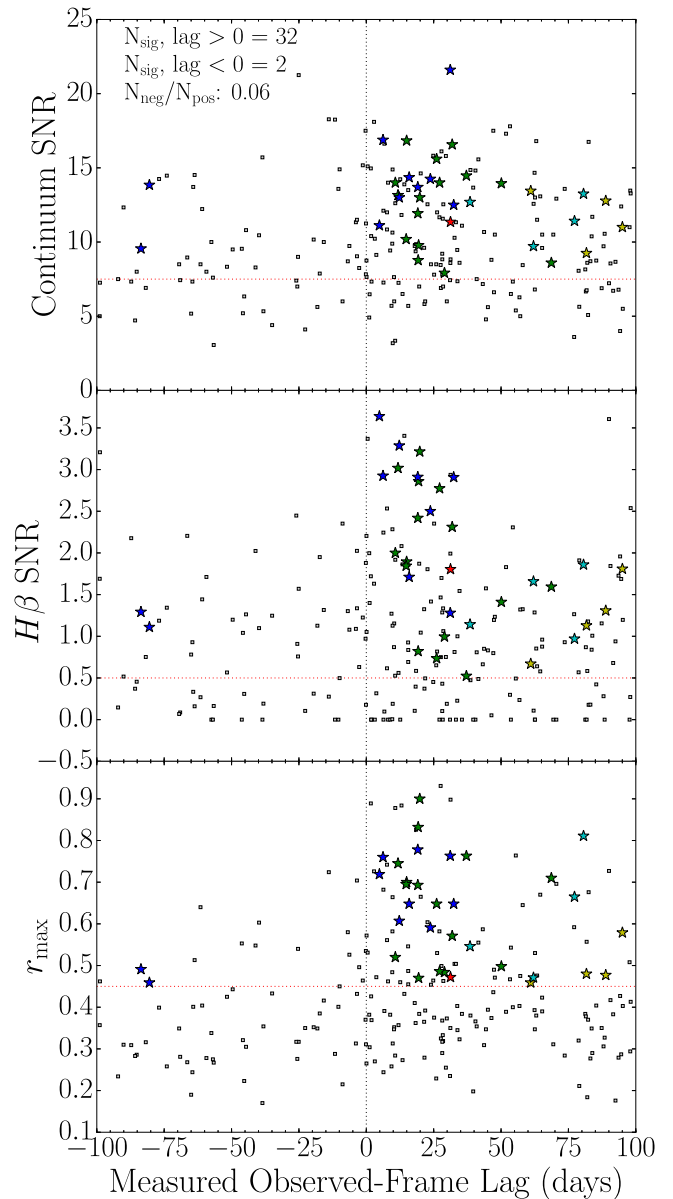


Figure 5. Measured time lags vs. parameters used to determine lag significance for our JAVELIN time-series analysis, as discussed in Section 3.3. The top panel shows the continuum light curve S/N above a linear trend, the middle panel shows the light curve variance S/N of the $H\beta$ light curves, and the bottom panel shows the maximum correlation coefficient of the ICCF, r_{max} . Lag measurements that were determined to be significant by our criteria are indicated by stars and are color coded by the quality rating assigned (see Section 3.5). Red, yellow, cyan, green, and blue represent measurements with assigned quality ratings of 1, 2, 3, 4, and 5, respectively (red and yellow are the lowest-quality measurements, while blue and green are the highest). The number of significant lags greater than and less than zero is indicated in the figure text. The black vertical dotted line shows a time lag of zero, and the red horizontal dotted line shows the cutoff threshold adopted for each parameter.

objects, but the lag measurements themselves were not well constrained, so they are excluded from our analysis.

Our false-positive rate is fairly stable to reasonable changes in the parameters used to determine lag significance. Altering the threshold for continuum light curve S/N (within the range of 6–8.5) changes the false-positive rate by less than 3% (which corresponds to just one additional false-positive measurement), and altering the line light curve S/N within the range of 0.3–0.8 changes the rate by less than a percent.

The false-positive rate is more sensitive to r_{\max} changes, as varying the r_{\max} threshold to values within the range of 0.1–0.5 alters the false-positive rate by 15%–20%. Despite the stability of the false-positive rate, all three criteria place important constraints on the quality of the reported lag measurements, and thus their primary utility is in rejecting poor measurements, both positive and negative.

Having established that the majority of our significant, positive-lag detections are likely to be real, we further restrict our significant-lag sample to only those lags that are greater than zero, as a negative lag is unphysical in terms of RM. Our significant-lag detections with $\tau > 0$, detected either by JAVELIN or CREAM, are reported in Table 3. We also present the light curves and their ICCFs, CCCDs, JAVELIN model fits, JAVELIN lag posterior distributions, CREAM fits, and CREAM posterior lag distributions in Figure sets 6 and 7 for all reported positive-lag detections.

3.4. Comparison between Different Lag-detection Methods

One of the aims of our study was to compare results from the three different time-series analysis methods (ICCF, JAVELIN, and CREAM). The top panel of Figure 8 shows that the JAVELIN and CREAM $H\beta$ lag measurements are consistent (within 1σ) for all but one object. Visual inspection of the outlier (RMID 622) indicates that the disagreement can be attributed to the presence of multiple peaks in the posterior distributions. There are peaks in the JAVELIN posteriors that match those from CREAM, but the peak strength ratios are reversed.

The agreement with the ICCF results is also generally quite good, as shown by the bottom panel of Figure 8. When the lag is considered detected with the ICCF method, the τ_{ICCF} measurements are generally consistent with both JAVELIN and CREAM (i.e., all three methods agree, as these are generally our strongest cases). In the quasars with (poorly detected) ICCF lags that differ from the JAVELIN and CREAM lags by $>1\sigma$, the posteriors of the different methods include the same peaks but at different strengths. The smaller uncertainties and larger number of well-detected lags with JAVELIN and CREAM are largely due to their use of the same (shifted, scaled, and smoothed) DRW model for both the continuum and broad-line light curves. In contrast, the ICCF assumes independent, linearly interpolated light curves for the continuum and broad lines. Well-measured light curves with high sampling result in nearly identical lag measurements from the ICCF and JAVELIN (as shown by Zu et al. 2011), and differences between the methods become apparent only for data sets like SDSS-RM with low cadence and noisy light curves.

Inspection of the light curves for quasars with mismatched ICCF lags (e.g., RMID 305 and 309 for $H\beta$, and RMID 779 for $H\alpha$) show that shifting the emission-line light curves by the JAVELIN and CREAM lags provides a better match to visual features repeated in both light curves than shifting by the ICCF lags does, so JAVELIN and CREAM appear to be more reliable. Jiang et al. (2017) have also run simulations with mock light curve data that suggest JAVELIN performs better than the ICCF in recovering true lags in the regime of sparsely sampled light curves. A full simulation comparing the detection completeness or efficiency for BLR lags among these different methods is currently underway (J. Li et al. 2017, in preparation). However, for our study, the above reasons and visual inspections of the light curves in Figures 6 and 7 support

the use of the JAVELIN and CREAM results for our main lag detections.

Using the same positive/negative lag fraction as a false-positive estimate, we find higher false-positive rates for CREAM and the ICCF than we did for JAVELIN. For CREAM, we measure a false-positive fraction of $16.7^{+7.3}_{-4.2}\%$ for $H\beta$ (42 positive, seven negative) and $11.8^{+12.2}_{-4.0}\%$ for $H\alpha$ (17 positive, two negative). For the ICCF, we measure a fraction of $25^{+13}_{-7.7}\%$ for $H\beta$ (16 positive, four negative), though we do not measure any significant negative $H\alpha$ lags and measure only eight positive lags, for a false-positive rate of zero (with an upper 1σ uncertainty of 18%).

3.5. Lag-measurement Quality

As suggested by our nonzero false-positive rates, it is statistically likely that a few of our lag measurements are false detections. Our objective criteria for significant-lag detection minimizes the false-positive rate and removes poor lag measurements, but does not eliminate the possibility for false detections entirely.

We tested the reliability of our lag estimates with a modified bootstrapping simulation, specifically to test whether or not our lag measurements are strongly dependent on the flux uncertainties of the light curves. For each light curve with N points, we randomly draw epochs N times with replacement, counting how many times each epoch is selected (n_{select}). The uncertainty on the flux of each epoch is then multiplied by $1/\sqrt{n_{\text{select}}}$ if it is selected at least once—if the epoch is not selected at all, its uncertainties are doubled. This is done 50 times for each source, creating 50 different iterations of both the continuum and $H\beta$ light curves. We then run our JAVELIN analysis on the light curves with the altered uncertainties and measure the lag.

From these simulations, we compare the distribution of recovered lags with the original lag measured from the unaltered light curves and determine what percentage are consistent with the original lag to within 1σ and 2σ . We naturally expect 68.3% of the resampled lags to be consistent to within 1σ and 95% to be consistent to within 2σ . On average, 81% of the bootstrap simulations are within 1σ of the original lag measurement, and 87% are within 2σ . This indicates that the JAVELIN lag estimates are robust against the uncertainties in the estimated errors in the light curve fluxes.

While we have shown that our lag measurements are generally robust, visual inspection leads us still to believe that some lags are more likely to be real than others, so we have assigned quality ratings to each of our lag measurements based on several different factors. The quality ratings range from 1 to 5, with 1 being the poorest-quality measurements and 5 being the highest-quality detections. When assigning these quality ratings, we paid particular attention to the following.

1. The unimodality of the posterior distribution: How smooth is this distribution? Are there many other peaks beyond the main peak, or perhaps a lot of low-level noise?
2. Agreement between different methods: Do all three methods (ICCF, CREAM, and JAVELIN) result in consistent lags? In about two-thirds of our detections, our procedure yielded detected lags using JAVELIN or CREAM but not using the ICCF. Our statistical analysis (e.g., Figure 5) indicates these lags are real in the

Table 3
SDSS-RM Observed-frame Lag Detections

RMID	z	H β Results					H α Results				
		τ_{CCF} (days)	τ_{JAV} (days)	τ_{CREAM} (days)	Quality ^a Rating	τ_{S16} ^b (days)	τ_{CCF} (days)	τ_{JAV} (days)	τ_{CREAM} (days)	Quality ^a Rating	
016	0.848	55.0 ^{+9.3} _{-9.2}	64.5 ^{+21.5} _{-34.6}	59.2 ^{+21.4} _{-28.6}	3	
017	0.456	32.7 ^{+15.4} _{-15.9}	37.1 ^{+15.8} _{-8.5}	36.7 ^{+4.3} _{-8.4}	4	...	65.3 ^{+20.0} _{-15.4}	82.4 ^{+10.6} _{-21.9}	65.7 ^{+3.6} _{-13.7}	5	
021	1.026	-86.0 ^{+10.0} _{-5.7}	88.9 ^{+9.9} _{-8.8}	-85.8 ^{+5.0} _{-3.4}	2	
033	0.715	19.0 ^{+20.4} _{-15.9}	47.7 ^{+11.0} _{-7.7}	45.5 ^{+16.9} _{-15.1}	1	
088	0.516	84.0 ^{+5.7} _{-8.3}	83.1 ^{+4.4} _{-7.7}	-82.0 ^{+3.6} _{-3.2}	3	
101	0.458	31.1 ^{+5.9} _{-11.4}	31.1 ^{+6.1} _{-9.3}	30.1 ^{+6.8} _{-8.4}	5	
160	0.359	14.6 ^{+8.9} _{-9.6}	31.3 ^{+8.1} _{-4.1}	29.8 ^{+5.7} _{-3.2}	3	...	16.5 ^{+10.3} _{-9.2}	27.7 ^{+5.3} _{-4.7}	28.5 ^{+1.9} _{-3.8}	4	
177	0.482	8.3 ^{+9.1} _{-6.6}	15.0 ^{+18.6} _{-4.0}	33.4 ^{+1.7} _{-24.3}	4	
191	0.442	14.0 ^{+5.7} _{-5.8}	12.2 ^{+3.6} _{-2.1}	11.0 ^{+3.1} _{-1.0}	5	33.6 ^{+3.9} _{-16.1}	26.0 ^{+9.6} _{-11.8}	24.0 ^{+5.9} _{-7.9}	24.2 ^{+4.8} _{-8.0}	4	
215	0.884	56.0 ^{+15.8} _{-16.4}	62.0 ^{+10.5} _{-9.6}	59.7 ^{+9.9} _{-10.4}	3	
229	0.470	21.0 ^{+6.3} _{-8.7}	23.8 ^{+4.3} _{-6.6}	23.0 ^{+4.7} _{-6.7}	5	...	34.0 ^{+19.1} _{-11.5}	32.5 ^{+11.3} _{-10.7}	31.3 ^{+8.3} _{-11.0}	3	
252	0.281	14.1 ^{+8.1} _{-6.7}	13.0 ^{+3.1} _{-2.5}	11.9 ^{+2.5} _{-1.8}	5	
265	0.734	15.8 ^{+10.9} _{-19.1}	14.8 ^{+5.6} _{-6.8}	14.4 ^{+5.7} _{-7.0}	4	
267	0.587	32.1 ^{+6.9} _{-5.5}	32.4 ^{+4.0} _{-3.2}	32.4 ^{+2.8} _{-3.2}	5	29.5 ^{+11.3} _{-6.0}	
272	0.263	21.1 ^{+7.5} _{-9.0}	19.1 ^{+4.0} _{-5.8}	19.5 ^{+1.8} _{-3.4}	5	27.7 ^{+10.0} _{-13.1}	42.2 ^{+24.0} _{-21.1}	40.7 ^{+19.7} _{-15.9}	40.2 ^{+13.4} _{-17.7}	3	
300	0.646	44.0 ^{+16.4} _{-16.3}	50.1 ^{+6.4} _{-13.6}	54.0 ^{+5.0} _{-10.4}	4	
301	0.548	21.4 ^{+10.7} _{-12.8}	19.8 ^{+8.9} _{-6.9}	19.0 ^{+4.1} _{-3.3}	4	
305	0.527	-74.0 ^{+22.2} _{-12.8}	81.7 ^{+6.4} _{-6.2}	81.7 ^{+4.1} _{-4.5}	2	
316	0.676	21.9 ^{+17.3} _{-20.3}	20.2 ^{+4.2} _{-3.1}	19.9 ^{+2.2} _{-1.7}	3	
320	0.265	33.9 ^{+10.1} _{-17.4}	31.9 ^{+5.9} _{-7.2}	35.4 ^{+1.8} _{-7.4}	4	37.4 ^{+3.2} _{-19.9}	25.9 ^{+18.7} _{-18.7}	25.7 ^{+18.0} _{-15.6}	25.6 ^{+13.3} _{-11.8}	4	
338	0.418	10.9 ^{+14.2} _{-12.8}	18.5 ^{+5.3} _{-9.7}	15.2 ^{+7.9} _{-6.3}	4	
371	0.472	9.5 ^{+12.9} _{-8.0}	10.8 ^{+11.7} _{-133.1}	19.2 ^{+2.1} _{-1.2}	3	...	19.4 ^{+14.8} _{-20.8}	33.5 ^{+1.3} _{-4.5}	33.3 ^{+0.9} _{-2.2}	3	
373	0.884	34.9 ^{+9.0} _{-11.1}	38.5 ^{+10.5} _{-13.1}	38.7 ^{+13.9} _{-11.3}	3	
377	0.337	12.0 ^{+16.0} _{-15.5}	7.7 ^{+0.8} _{-1.0}	7.8 ^{+0.6} _{-0.7}	3	...	7.1 ^{+14.3} _{-44.0}	7.9 ^{+1.2} _{-1.4} & 7.7 ^{+0.6} _{-0.7}	2	...	
392	0.843	27.1 ^{+6.5} _{-12.5}	26.1 ^{+6.7} _{-5.5}	26.3 ^{+4.1} _{-4.2}	4	
399	0.608	15.0 ^{+20.7} _{-11.2}	58.0 ^{+1.9} _{-1.3}	57.6 ^{+1.8} _{-16.5}	2	
428	0.976	-80.0 ^{+11.4} _{-11.2}	31.2 ^{+11.9} _{-3.7}	32.3 ^{+24.3} _{-7.5}	1	
457	0.604	24.0 ^{+9.2} _{-21.9}	24.0 ^{+6.0} _{-13.9}	25.0 ^{+5.2} _{-8.2}	3	
519	0.554	0.0 ^{+4.6} _{-6.2}	19.4 ^{+2.9} _{-4.1}	19.5 ^{+1.5} _{-2.8}	4	
551	0.680	12.9 ^{+25.4} _{-11.7}	10.8 ^{+2.5} _{-2.4}	10.7 ^{+2.8} _{-2.6}	4	
589	0.751	69.0 ^{+18.7} _{-14.4}	80.6 ^{+16.7} _{-16.6}	96.2 ^{+2.9} _{-18.1}	3	
601	0.658	8.8 ^{+23.4} _{-18.5}	19.2 ^{+14.2} _{-7.7}	19.2 ^{+11.2} _{-7.4}	4	
622	0.572	76.0 ^{+19.5} _{-13.2}	77.3 ^{+17.5} _{-3.2}	32.9 ^{+9.6} _{-1.8}	3	
634	0.650	38.1 ^{+15.8} _{-19.7}	29.0 ^{+14.2} _{-12.2}	29.4 ^{+12.6} _{-8.9}	4	
645	0.474	7.5 ^{+9.5} _{-12.5}	27.6 ^{+5.2} _{-172.4}	30.6 ^{+1.3} _{-4.4}	4	20.9 ^{+9.6} _{-11.9}	26.7 ^{+9.4} _{-22.9}	35.7 ^{+15.1} _{-7.7}	33.9 ^{+14.7} _{-5.4}	5	
694	0.532	13.1 ^{+13.4} _{-15.7}	15.9 ^{+9.6} _{-4.6}	15.8 ^{+9.8} _{-4.0}	5	21.6 ^{+19.8} _{-14.6}	
707	0.890	0.0 ^{+8.5} _{-15.7}	68.7 ^{+8.5} _{-10.5}	82.7 ^{+4.6} _{-10.8}	4	
720	0.467	66.0 ^{+11.9} _{-15.4}	61.0 ^{+21.7} _{-12.2}	59.9 ^{+19.6} _{-9.6}	2	
733	0.455	74.0 ^{+13.9} _{-21.8}	77.0 ^{+12.7} _{-8.2}	-84.2 ^{+13.0} _{-11.4}	2	
768	0.258	42.0 ^{+17.8} _{-13.0}	52.9 ^{+3.4} _{-2.7}	52.7 ^{+3.5} _{-1.4}	5	
772	0.249	1.3 ^{+4.7} _{-5.2}	4.9 ^{+1.1} _{-1.1}	5.0 ^{+0.8} _{-0.6}	5	...	9.0 ^{+4.3} _{-7.0}	7.4 ^{+2.0} _{-1.2}	7.4 ^{+1.0} _{-0.9}	5	
775	0.172	22.1 ^{+10.2} _{-12.9}	19.1 ^{+15.4} _{-7.7}	17.5 ^{+14.1} _{-6.3}	4	22.5 ^{+5.0} _{-15.0}	
776	0.116	10.0 ^{+6.3} _{-4.2}	11.8 ^{+1.1} _{-2.4}	12.3 ^{+0.9} _{-2.9}	4	...	8.0 ^{+5.4} _{-6.3}	9.2 ^{+5.5} _{-2.6}	9.3 ^{+3.4} _{-2.0}	4	
779	0.152	12.1 ^{+9.5} _{-10.1}	13.1 ^{+1.7} _{-3.4}	13.5 ^{+0.8} _{-1.8}	4	...	16.9 ^{+21.6} _{-13.7}	92.4 ^{+5.7} _{-7.2}	92.0 ^{+6.0} _{-15.4}	2	
781	0.263	93.0 ^{+3.1} _{-10.5}	95.0 ^{+4.0} _{-4.1}	95.4 ^{+3.6} _{-3.1}	2	
782	0.362	15.0 ^{+14.4} _{-6.8}	27.2 ^{+1.5} _{-4.1}	27.3 ^{+1.8} _{-2.1}	4	
790	0.237	11.0 ^{+6.1} _{-6.5}	9.8 ^{+5.2} _{-5.2}	6.8 ^{+7.1} _{-2.6}	3	...	0.9 ^{+11.9} _{-5.6}	55.7 ^{+27.6} _{-4.8}	55.6 ^{+29.3} _{-4.8}	2	
840	0.244	8.1 ^{+3.4} _{-2.3}	6.2 ^{+1.9} _{-1.7}	6.1 ^{+1.8} _{-1.2}	5	13.6 ^{+26.0} _{-8.2}	11.9 ^{+5.6} _{-3.7}	13.2 ^{+2.9} _{-3.0}	12.9 ^{+2.5} _{-2.4}	5	

Notes.^a Lag quality rating (see Section 3.5).^b The lag measured by Shen et al. (2016b), for comparison purposes.

statistical sense. The ICCF is likely less powerful in detecting lags in cases where we have lower S/N or lower-cadence light curves, so generally we prefer

agreement between CREAM and JAVELIN only. However, if the ICCF results are also consistent, this likely indicates a more solid measurement, so we take this

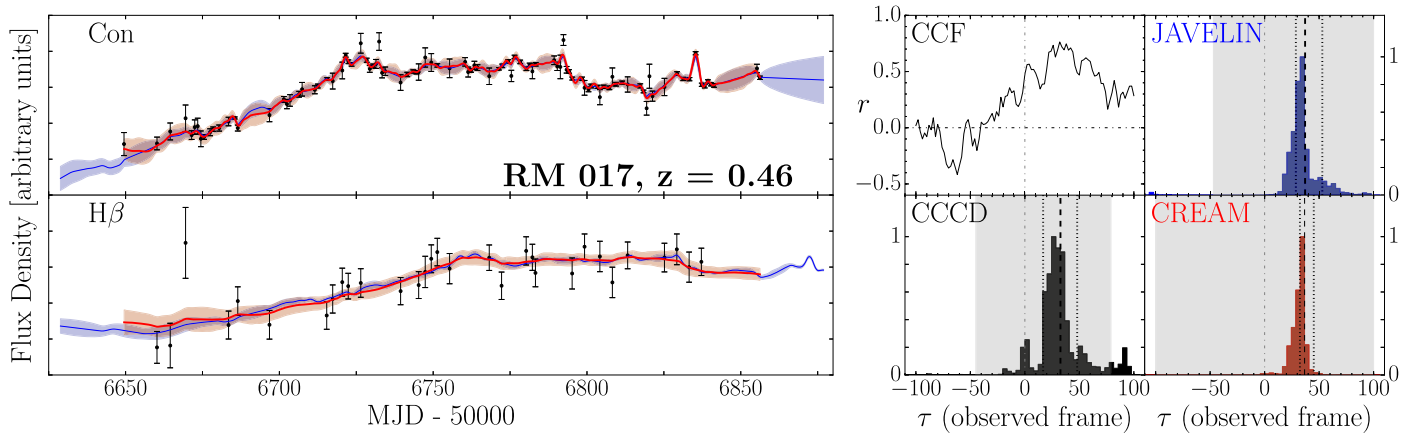


Figure 6. Light curves and models for the $H\beta$ emission-line analysis of SDSS J141324.28+530527.0 (RMID 017, $z = 0.46$). The continuum and $H\beta$ light curves are presented in the top and bottom of the left panels. For display purposes, we show the weighted mean of all epochs observed within a single night. The JAVELIN model and the uncertainty envelope are given in blue, and the CREAM models and their uncertainties in red. The right four panels show the results of the time-series analysis. The top left panel shows the CCF. The other three panels present the lag distributions for the three different methods, normalized to the tallest peak in the distribution. The bottom left panel shows the CCFD, the top right panel shows the JAVELIN posterior lag distribution, and the bottom right panel shows the CREAM posterior lag distribution. Black vertical dashed and dotted lines correspond to the measured observed-frame lag and its uncertainties. The gray dash-dotted vertical lines indicate a lag of zero to guide the eye, and the horizontal dash-dotted line in the CCF panel shows a cross-correlation coefficient r of 0. The gray shaded area covers the regions of the posteriors that were included in the measurements, as determined during the alias rejection procedure (see Section 3.2). The other figures for each source are in the figure set.

(The complete figure set (44 images) is available.)

into account when evaluating the quality of these measurements.

3. Light curve variability: Are there apparent short-term variability features in the continuum light curve that are also apparent in the emission-line light curve? Can we identify the lag by eye? Does the reported lag look reasonable if we shift the emission-line light curve by this lag?
4. Model fit quality: How well do the JAVELIN and CREAM model light curves match the observed light curve? Are the two model light curves in agreement with one another?
5. Bootstrapping results: What is the fraction of consistent samples from the bootstrapping described above? If enough samples are inconsistent with our original lag measurement, this indicates that the lag is less reliable, and the object is given a lower quality rating.

We include our quality assessments for each lag measurement in Table 3. We recognize that these are subjective. However, they are based on our significant past experience with RM measurements, and thus we provide them to help the reader evaluate the results.

4. Results and Discussion

4.1. Lag Results

Inspection of the light curves and posterior distributions of sources with lags that were detected by CREAM and not JAVELIN reveals that JAVELIN has a tendency to find more aliases than CREAM, particularly in light curves with a longer-term monotonic trend present in the light curve. Despite our alias-removal procedure, the presence of these aliases can cause the measurement to fail our significance criteria despite JAVELIN having measured a lag similar to CREAM. For our final τ measurements, we thus adopt τ_{JAV} if the lag was detected by JAVELIN and τ_{CREAM} for the quasars in which the

lag was detected by CREAM but not JAVELIN. We hereafter refer to the final adopted τ (which is equivalent to either τ_{JAVELIN} or τ_{CREAM}) as τ_{final} . This procedure yields 32 $H\beta$ lags from JAVELIN alone, and we add 12 more $H\beta$ lags from CREAM, yielding a total of 44 $H\beta$ lags. Based on the $H\beta$ false-positive rates estimated for each method (see Sections 3.3 and 3.4), we expect two false positives among the JAVELIN lags and two false positives among the CREAM lags, yielding an overall number of expected false positives of four out of 44 measurements ($9.1^{+5.6}_{-1.9}\%$). In addition, we measured 13 $H\alpha$ lags from JAVELIN and add five $H\alpha$ lags from CREAM, yielding 18 total $H\alpha$ lag measurements. Based on the $H\alpha$ false-positive rate, we expect one false positive from JAVELIN and less than one from CREAM, yielding an expected 1.59 out of 18 $H\alpha$ lags ($8.8^{+10.7}_{-2.2}\%$). We provide rest-frame τ_{final} measurements for all sources with detected lags in either $H\beta$ or $H\alpha$ in Tables 4 and 5 and show the luminosity–redshift distribution of these sources in Figure 9. We have expanded the redshift range of the RM sample out to $z \sim 1$ and increased the number of lag measurements in the sample by about two-thirds.

Shen et al. (2016b), hereafter S16, report nine $H\beta$ lags from the SDSS-RM sample measured from only the spectroscopic light curves. We detect eight of them here and provide the original measurements from S16 (denoted τ_{S16} and corrected to the observed frame) in Table 3 for comparison. Our measurements for the eight detections are all consistent with theirs, but with lower uncertainties due to our addition of the photometric light curves (see Table 3). We find a significantly lower lag for RM 191; this is likely because of the increased cadence of our continuum light curves when the photometric monitoring was incorporated. Because of the increased cadence, we are sensitive to shorter lags and thus are able to measure the shorter lag in this object. The only source detected by S16 that we do not detect a lag for is RM 769. In our case, all three methods yielded lags that were positive but formally consistent with zero to within the uncertainties. Again, the increased cadence of the light curves is responsible for the

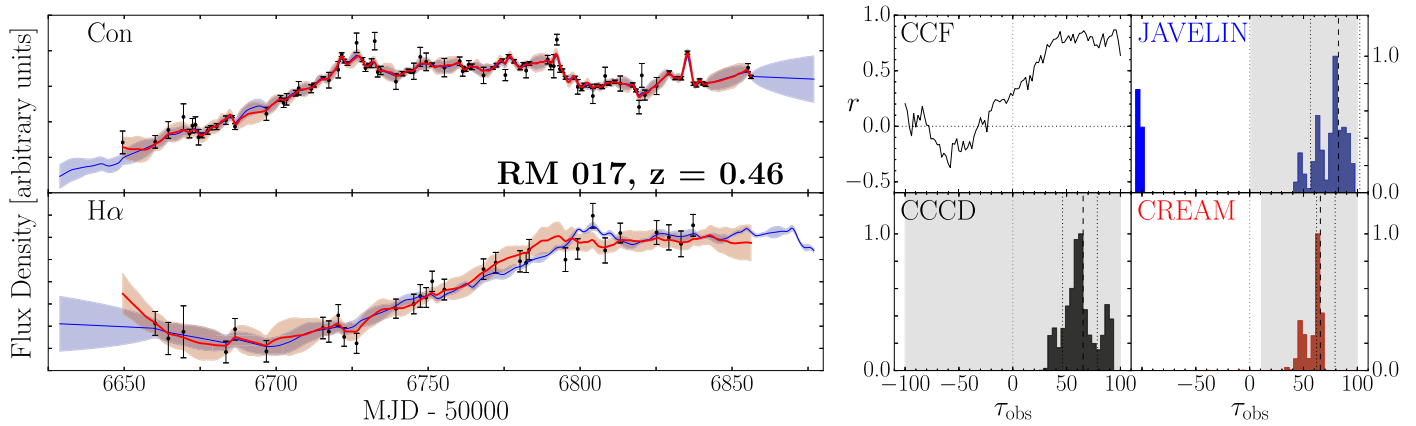


Figure 7. Light curves and output for the $H\alpha$ time-series analysis for SDSS J141324.28+530527.0 (RM 017, $z = 0.456$). Lines and symbols are the same as in Figure 6. The other figures for each source are in the figure set.

(The complete figure set (17 images) is available.)

difference, allowing us to see that the lag is not well constrained for this source.

In 14 quasars, we measure significant lags for both $H\beta$ and $H\alpha$; Figure 10 compares the $H\beta$ and $H\alpha$ lags for those objects. We see that in all cases, the $H\alpha$ lag is consistent with or larger than the $H\beta$ lag; this was also reported in previous studies (e.g., Kaspi et al. 2000; Bentz et al. 2010). Larger $H\alpha$ lags are expected due to photoionization predictions, with radial stratification and optical-depth effects causing the $H\alpha$ emission line to appear at larger distances than $H\beta$ (Netzer 1975; Rees et al. 1989; Korista & Goad 2004); see Section 4.3 of Bentz et al. (2010) for a more detailed discussion of this phenomenon.

Shen et al. (2015b) computed the average 5100 Å luminosity of most of our sources during the same monitoring period using spectral decomposition to remove host-galaxy light, allowing us to place these sources on the $R-L$ relation; we provide these luminosities in Table 1. Figure 11 presents the $R-L$ relationship measured by Bentz et al. (2013) and shows the location of our new $H\beta$ lag measurements. Figure 11 also shows previous RM data from Du et al. (2016b) and the compilation of Bentz & Katz (2015). For a consistent comparison with our SDSS-RM measurements, we use JAVELIN lags when available from the Bentz & Katz (2015) database. Many of the lags (including the Du et al. 2016b data) were measured with the ICCF and so typically have larger uncertainties than JAVELIN measurements. However, the lag values themselves are consistent with ICCF measurements, and thus there are no issues when comparing measurements made with the various methods. Differences in our lag-measuring procedure (such as adopting the median of the CCCD) also yield measurements that are consistent with those using previously favored procedures, and thus these lag measurements can also be compared to lags from prior studies without issue.

Both our data and the Du et al. (2016b) super-*eddington* accreting massive black holes (SEAMBHs) sample have many AGNs that lie below the $R-L$ relation and its expected scatter. A similar offset from the expected $R-L$ relation was measured for the SDSS-RM quasars using composite cross-correlation methods (Li et al. 2017). At least some of the disagreement may be due to selection effects: the SDSS-RM 2014 cadence and monitoring duration limit our lag detections to less than ~ 100 days in the observed frame, and it is more difficult to measure the longer lags even below this limit, so we are less likely to

measure lags that scatter above the $R-L$ relation. (The observations had similar cadence and duration.)

It is also possible that this offset is due to physical dependencies in the $R-L$ relation. Both the SDSS-RM and SEAMBH quasars lie at the mid-to-high-luminosity end of the L distribution of the Bentz & Katz (2015) sample of RM quasars, and it is possible that luminous quasars have different BLR radii than expected from the $R-L$ relation established from low-luminosity AGN. Du et al. (2016b) argue that the offset is caused by high accretion rates, since the most rapidly accreting SEAMBH quasars tend to be more frequently offset. We tested this hypothesis by calculating the accretion rate using the same parameterization as Du et al. (2016a, their Equation (13)). In general, our SDSS-RM quasars have much ($10-1000\times$) lower accretion rates than the Du et al. (2016b) sample (although our quasars have similar L and R , they have broader line widths than the narrow-line type 1 AGNs in the SEAMBH sample). The SDSS-RM sample also does not show a clear trend between $R-L$ offset and accretion rate. It is possible that the $R-L$ offset is driven by luminosity rather than accretion rate, or by other quasar properties in which the previous RM samples were biased (e.g., Shen et al. 2015a). Fully exploring the deviations from the $R-L$ relationship will require the multiyear SDSS-RM data or careful simulations of the observational biases in order to rule out selection effects. We thus defer more detailed discussion of the $R-L$ relation to future work.

Our full sample contains 222 quasars; we have thus been able to detect lags in about 20% of them. Typical yields for traditional RM campaigns with single-object spectrographs (e.g., Fausnaugh et al. 2017) are on the order of 50%; failure in such campaigns, which obtain very high-quality data at high cadences, is usually attributed to a lack of favorable variability behavior of the quasars. These campaigns achieve this 50% fraction through object selection (the AGNs are chosen to have strong emission lines and often are already known to show strong variability), high observing cadence (usually once per day), and high-S/N spectra. Our sample is more representative of quasars with a variety of emission-line properties and luminosities; we thus do not expect as many of our sources to vary in a favorable manner (short-term, high-amplitude variations) during the campaign. In addition, our sample is much fainter on average, which makes flux variations more difficult to detect. The cadence and length of the campaign also

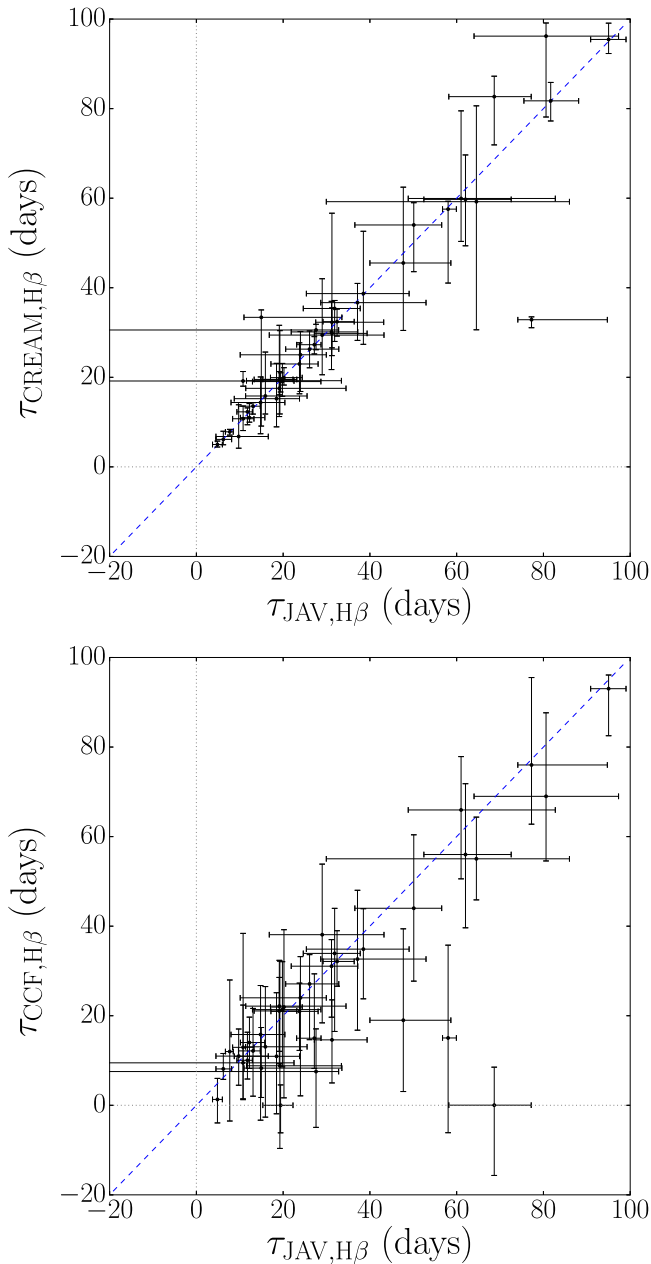


Figure 8. Comparison of the observed-frame $H\beta$ τ_{CREAM} and τ_{JAV} measurements (top panel), and the τ_{JAV} and τ_{CCF} measurements (bottom panel). In both panels, the blue dashed line shows a ratio of one-to-one. Gray dotted lines indicate time lags of zero along both axes to guide the eye.

affect the yield; we are unable to detect lags longer than ~ 100 days in the observed frame, which means that lags for the higher-luminosity quasars in our sample (expected to have $H\beta$ time lags of up to ~ 300 days in the observed frame) are undetectable with this data set. We expect that future programs similar to SDSS-RM will similarly yield a $\sim 20\%$ detection fraction over the first year (although the fraction may be higher for a brighter subset of quasars), with improvements if the overall cadence and monitoring length are increased.

4.2. Black Hole Mass Measurements

We use our τ_{final} measurements in combination with line-width measurements from PrepSpec to compute M_{BH} for our sources following Equation (1). We report these line-width

measurements, along with the adopted lags, calculated virial products, and M_{BH} measurements, for $H\beta$ in Table 4 and $H\alpha$ in Table 5. To calculate the virial products, we use $\sigma_{\text{line,rms}}$ measured from the rms residual spectrum, which has been shown to be a less biased estimator for M_{BH} than the FWHM for $H\beta$ -based measurements (Peterson 2011). We note that the PrepSpec rms spectrum is different from “traditional” rms spectra used in many previous studies (e.g., Kaspi et al. 2000; Peterson et al. 2004). Most prior studies include the entire spectrum, including the continuum and any blended components, in the rms spectrum computation. PrepSpec decomposes the spectra into multiple components, and the rms line profiles are measured from the broad-line model only. The resulting rms widths are different from those measured from the entire spectrum. Barth et al. (2015) examined possible sources of systematics in the rms line-width measurements and found that the inclusion of the continuum in the rms calculation can cause the line widths to be underestimated (see Barth et al. 2015, Appendix C, for details).

We propagate the uncertainties in τ_{JAV} and σ_{line} to compute the statistical uncertainties on the virial product; however, there are additional systematic uncertainties affecting M_{BH} measurements that have not yet been taken into account. Fausnaugh et al. (2017) calculate a 0.16 dex standard deviation in the mass of the BH in NGC 5548, which has been measured by many independent monitoring campaigns over the past 30 years (Bentz & Katz 2015). We follow Fausnaugh et al. (2017) and add 0.16 dex uncertainties in quadrature with the statistical uncertainties in the virial product to produce our final adopted uncertainties. We adopt a scale factor $f = 4.47$ (Woo et al. 2015) to convert the virial products to M_{BH} . We note that the 0.16 dex systematic uncertainty is negligible compared to the systematic uncertainty in the virial scale factor f (generally recognized to be on the order of 0.4 dex).

We also compare our M_{BH} measurements ($M_{\text{BH,RM}}$) from the $H\beta$ emission line with those measured by Shen et al. (2015b) using single-epoch spectra and the prescription of Vestergaard & Peterson (2006), hereafter VP06, for objects with 5100 \AA luminosity measurements ($M_{\text{BH,SE}}$). Before comparing measurements, however, we increased the reported statistical uncertainties of the single-epoch measurements by 0.43 dex to account for the intrinsic scatter measured by VP06 in the single-epoch M_{BH} calibration. VP06 used a higher scaling factor than our adopted value, which results in slightly higher (by 0.1 dex) single-epoch masses (VP06 adopt $f_{\sigma} = 5.5$ and $f_{\text{FWHM}} = 1.4$ from Onken et al. 2004, while we adopt $f_{\sigma} = 4.47$ and $f_{\text{FWHM}} = 1.12$ from Woo et al. 2015).

Figure 12 shows a comparison between the two measurements. In most cases, our M_{BH} measurements are consistent with the single-epoch measurements given the uncertainties. The agreement is even better if a correction is applied for the different scaling factor. The scatter around a one-to-one relation among our sample is similar to the scatter seen among the Bentz & Katz (2015) and Du et al. (2016b) samples. However, both our sample and that of Du et al. (2016b) have slightly overmassive single-epoch M_{BH} at low RM masses. This is consistent with the deviation seen from the $R-L$ relation (Figure 11), with smaller RM lags than expected from luminosity and the Bentz et al. (2013) relation. As before, it is possible that the differences are associated with differences in quasar properties: our sources are more luminous than those of Bentz et al. (2013), though not as rapidly accreting as the

Table 4
Line Width, Virial Product, and M_{BH} Measurements for H β

RMID	z	$\tau_{\text{final}}^{\text{a}}$ (days)	$\sigma_{\text{line,mean}}^{\text{b}}$ (km s $^{-1}$)	$\sigma_{\text{line,rms}}^{\text{b}}$ (km s $^{-1}$)	$\text{FWHM}_{\text{mean}}^{\text{b}}$ (km s $^{-1}$)	$\text{FWHM}_{\text{rms}}^{\text{b}}$ (km s $^{-1}$)	VP ($10^7 M_{\odot}$)	M_{BH}^{c} ($10^7 M_{\odot}$)	σ_{*}^{d} (km s $^{-1}$)
RM 016	0.848	$32.0_{-15.5}^{+11.6}$	4585 ± 50	6477 ± 54	7976 ± 42	7859 ± 112	$26.2_{-13.3}^{+10.4}$	$117.3_{-59.7}^{+46.3}$...
RM 017	0.456	$25.5_{-5.8}^{+10.9}$	6937 ± 14	6101 ± 48	16318 ± 30	7758 ± 77	$18.5_{-5.2}^{+8.4}$	$82.8_{-23.1}^{+37.6}$	191.4 ± 3.7
RM 021	1.026	$43.9_{-4.3}^{+4.9}$	4856 ± 536	6543 ± 34	7442 ± 5983	11002 ± 1743	$36.6_{-6.9}^{+7.2}$	$163.8_{-30.8}^{+32.0}$...
RM 033	0.715	$26.5_{-8.8}^{+9.9}$	776 ± 13	857 ± 32	1070 ± 30	1626 ± 243	$0.4_{-0.1}^{+0.2}$	$1.7_{-0.6}^{+0.7}$	182.4 ± 21.7
RM 101	0.458	$21.4_{-6.4}^{+4.2}$	1186 ± 2	976 ± 32	2220 ± 9	2135 ± 94	$0.4_{-0.1}^{+0.1}$	$1.8_{-0.6}^{+0.4}$...
RM 160	0.359	$21.9_{-2.4}^{+4.2}$	1773 ± 6	1909 ± 12	4399 ± 31	4183 ± 51	$1.6_{-0.3}^{+0.4}$	$7.0_{-1.3}^{+1.7}$...
RM 177	0.482	$10.1_{-2.7}^{+12.5}$	2541 ± 9	2036 ± 39	5277 ± 39	4930 ± 163	$0.8_{-0.3}^{+1.0}$	$3.7_{-1.1}^{+4.6}$	171.5 ± 10.7
RM 191	0.442	$8.5_{-1.4}^{+2.5}$	845 ± 12	1030 ± 18	1316 ± 94	1967 ± 76	$0.2_{-0.0}^{+0.1}$	$0.8_{-0.2}^{+0.3}$	152.0 ± 8.5
RM 215	0.884	$32.9_{-5.1}^{+5.6}$	7078 ± 47	7681 ± 64	13980 ± 1935	21468 ± 2120	$37.9_{-8.4}^{+8.8}$	$169.4_{-37.7}^{+39.5}$...
RM 229	0.470	$16.2_{-4.5}^{+2.9}$	1722 ± 18	1781 ± 38	3055 ± 180	2377 ± 288	$1.0_{-0.3}^{+0.2}$	$4.5_{-1.4}^{+1.1}$	130.2 ± 8.7
RM 265	0.734	$8.5_{-3.9}^{+3.2}$	5881 ± 103	7165 ± 36	4509 ± 71	11017 ± 109	$8.5_{-4.2}^{+3.5}$	$38.2_{-18.6}^{+15.7}$...
RM 267	0.587	$20.4_{-2.0}^{+2.5}$	1305 ± 6	1202 ± 33	2647 ± 23	1998 ± 75	$0.6_{-0.1}^{+0.1}$	$2.6_{-0.5}^{+0.5}$	97.1 ± 9.0
RM 272	0.263	$15.1_{-4.6}^{+3.2}$	1465 ± 2	1697 ± 10	2465 ± 30	4064 ± 102	$0.9_{-0.3}^{+0.2}$	$3.8_{-1.3}^{+1.0}$...
RM 300	0.646	$30.4_{-8.3}^{+3.9}$	1153 ± 8	1232 ± 30	2110 ± 36	2553 ± 136	$0.9_{-0.3}^{+0.2}$	$4.0_{-1.3}^{+0.8}$	109.4 ± 11.9
RM 301	0.548	$12.8_{-4.5}^{+5.7}$	7061 ± 25	6259 ± 23	18920 ± 91	10477 ± 114	$9.8_{-3.8}^{+4.7}$	$43.8_{-16.8}^{+20.8}$	176.9 ± 10.1
RM 305	0.527	$53.5_{-4.0}^{+4.2}$	2331 ± 7	2126 ± 35	2616 ± 21	3172 ± 85	$4.7_{-0.8}^{+0.8}$	$21.1_{-3.7}^{+3.8}$	150.5 ± 7.7
RM 316	0.676	$11.9_{-1.0}^{+1.3}$	4686 ± 12	7195 ± 40	3742 ± 6	13483 ± 141	$12.0_{-2.2}^{+2.3}$	$53.7_{-9.7}^{+10.5}$...
RM 320	0.265	$25.2_{-5.7}^{+4.7}$	1569 ± 9	1462 ± 26	3917 ± 28	2718 ± 80	$1.1_{-0.3}^{+0.3}$	$4.7_{-1.3}^{+1.1}$	66.4 ± 4.6
RM 338	0.418	$10.7_{-4.4}^{+5.6}$	2670 ± 28	2291 ± 33	4701 ± 610	5136 ± 226	$1.1_{-0.5}^{+0.6}$	$4.9_{-2.2}^{+2.7}$	83.3 ± 8.3
RM 371	0.472	$13.0_{-0.8}^{+1.4}$	1484 ± 6	1443 ± 11	3458 ± 55	4123 ± 40	$0.5_{-0.1}^{+0.1}$	$2.4_{-0.4}^{+0.5}$...
RM 373	0.884	$20.4_{-7.0}^{+5.6}$	1726 ± 19	2491 ± 26	5582 ± 128	7211 ± 727	$2.5_{-0.9}^{+0.8}$	$11.1_{-4.2}^{+3.5}$...
RM 377	0.337	$5.9_{-0.6}^{+0.4}$	1648 ± 16	1789 ± 23	3555 ± 42	5654 ± 239	$0.4_{-0.1}^{+0.1}$	$1.6_{-0.3}^{+0.3}$	115.3 ± 4.6
RM 392	0.843	$14.2_{-3.0}^{+3.7}$	3120 ± 46	3658 ± 56	3540 ± 199	10839 ± 153	$3.7_{-1.0}^{+1.1}$	$16.5_{-4.4}^{+5.0}$	77.2 ± 25.6
RM 399	0.608	$35.8_{-10.3}^{+1.1}$	1429 ± 23	1619 ± 38	2675 ± 60	2578 ± 112	$1.8_{-0.6}^{+0.3}$	$8.2_{-2.7}^{+1.3}$	187.2 ± 7.8
RM 428	0.976	$15.8_{-1.9}^{+6.0}$	6913 ± 12	7568 ± 70	11219 ± 23	7156 ± 61	$17.7_{-3.5}^{+7.3}$	$79.0_{-15.8}^{+32.7}$...
RM 457	0.604	$15.6_{-5.1}^{+3.2}$	2988 ± 83	2788 ± 48	6404 ± 424	7451 ± 221	$2.4_{-0.9}^{+0.6}$	$10.6_{-3.9}^{+2.8}$	110.0 ± 18.4
RM 519	0.554	$12.5_{-2.6}^{+1.8}$	7008 ± 200	9475 ± 33	3740 ± 141	17614 ± 153	$21.9_{-5.8}^{+4.8}$	$97.8_{-25.9}^{+21.3}$...
RM 551	0.680	$6.4_{-1.4}^{+1.5}$	1194 ± 11	1298 ± 36	1887 ± 59	1638 ± 113	$0.2_{-0.1}^{+0.1}$	$0.9_{-0.3}^{+0.3}$...
RM 589	0.751	$46.0_{-9.5}^{+9.5}$	5424 ± 57	5013 ± 49	4553 ± 79	7625 ± 136	$22.6_{-5.9}^{+5.9}$	$100.9_{-26.3}^{+26.4}$...
RM 601	0.658	$11.6_{-4.6}^{+8.6}$	6705 ± 58	5284 ± 54	16168 ± 354	12673 ± 455	$6.3_{-2.7}^{+4.8}$	$28.3_{-12.2}^{+21.3}$	214.9 ± 19.2
RM 622	0.572	$49.1_{-2.0}^{+11.1}$	1369 ± 6	1423 ± 32	2565 ± 36	3234 ± 164	$1.9_{-0.3}^{+0.5}$	$8.7_{-1.4}^{+2.4}$	122.9 ± 9.2
RM 634	0.650	$17.6_{-7.4}^{+8.6}$	1059 ± 25	1527 ± 22	1154 ± 42	3422 ± 491	$0.8_{-0.4}^{+0.4}$	$3.6_{-1.6}^{+1.8}$	119.4 ± 20.9
RM 645	0.474	$20.7_{-3.0}^{+0.9}$	1544 ± 7	1438 ± 17	3588 ± 56	3810 ± 67	$0.8_{-0.2}^{+0.1}$	$3.7_{-0.8}^{+0.6}$...
RM 694	0.532	$10.4_{-3.0}^{+6.3}$	845 ± 4	740 ± 23	1501 ± 17	1693 ± 98	$0.1_{-0.0}^{+0.1}$	$0.5_{-0.2}^{+0.3}$...
RM 707	0.890	$36.3_{-5.5}^{+4.5}$	989 ± 20	1252 ± 11	1552 ± 95	2752 ± 90	$1.1_{-0.2}^{+0.2}$	$5.0_{-1.1}^{+1.0}$...
RM 720	0.467	$41.6_{-8.3}^{+14.8}$	1346 ± 4	1232 ± 16	3130 ± 23	3131 ± 44	$1.2_{-0.3}^{+0.5}$	$5.5_{-1.4}^{+2.1}$...
RM 772	0.249	$3.9_{-0.9}^{+0.9}$	1065 ± 14	1026 ± 14	2439 ± 33	2078 ± 35	$0.1_{-0.0}^{+0.0}$	$0.4_{-0.1}^{+0.1}$	136.5 ± 3.1
RM 775	0.172	$16.3_{-6.6}^{+13.1}$	1578 ± 5	1818 ± 8	3072 ± 24	5010 ± 61	$1.1_{-0.5}^{+0.9}$	$4.7_{-2.0}^{+3.9}$	130.4 ± 2.6
RM 776	0.116	$10.5_{-2.2}^{+1.0}$	1501 ± 5	1409 ± 11	3700 ± 16	3111 ± 36	$0.4_{-0.1}^{+0.1}$	$1.8_{-0.5}^{+0.3}$	112.4 ± 1.9
RM 779	0.152	$11.8_{-1.5}^{+0.7}$	1249 ± 4	1205 ± 9	2670 ± 17	2709 ± 55	$0.3_{-0.1}^{+0.1}$	$1.5_{-0.3}^{+0.3}$	57.1 ± 4.9
RM 781	0.263	$75.2_{-3.3}^{+3.2}$	1169 ± 5	1089 ± 22	2515 ± 26	3340 ± 82	$1.7_{-0.3}^{+0.3}$	$7.8_{-1.3}^{+1.3}$	104.7 ± 4.3
RM 782	0.362	$20.0_{-3.0}^{+1.1}$	1378 ± 6	1353 ± 23	3070 ± 49	2730 ± 137	$0.7_{-0.2}^{+0.1}$	$3.2_{-0.7}^{+0.5}$	129.5 ± 6.7
RM 790	0.237	$5.5_{-2.1}^{+5.7}$	6813 ± 13	6318 ± 38	17112 ± 81	9448 ± 367	$4.3_{-1.8}^{+4.5}$	$19.1_{-8.0}^{+20.2}$	204.4 ± 3.1
RM 840	0.244	$5.0_{-1.4}^{+1.5}$	6596 ± 22	4457 ± 60	15735 ± 93	6580 ± 48	$1.9_{-0.6}^{+0.7}$	$8.6_{-2.7}^{+3.0}$	164.3 ± 3.6

Notes.

^a Measurements are in the quasar rest frame. If the lag is detected by JAVELIN, we use the JAVELIN-reported lag by default; otherwise, we use the CREAM-reported lag.

^b Line widths are measured using PrepSpec. The mean line widths are measured from the broad component only, and the rms line widths do not include the continuum.

^c Virial products were converted to M_{BH} using $f = 4.47$, as measured by Woo et al. (2015).

^d From Shen et al. (2015b).

Du et al. (2016b) quasars. However, it is also possible that the apparent deviation is caused by selection effects associated with our limited cadence and duration, so we withhold definitive conclusions until detailed simulations of the observational biases are examined in future work.

We also compare our M_{BH} measurements from H β with those from H α in Figure 13, and we find that the measurements are consistent to within the uncertainties for nearly all sources.

Figure 14 places our M_{BH} measurements on the $M_{\text{BH}}-\sigma_{*}$ relationship. These σ_{*} measurements were taken from Shen

Table 5
Line Width, Virial Product, and M_{BH} Measurements for $\text{H}\alpha$

RMID	z	$\tau_{\text{final}}^{\text{a}}$ (days)	$\sigma_{\text{line,mean}}$ (km s^{-1})	$\sigma_{\text{line,rms}}$ (km s^{-1})	$\text{FWHM}_{\text{mean}}$ (km s^{-1})	FWHM_{rms} (km s^{-1})	VP ($10^7 M_{\odot}$)	M_{BH}^{b} ($10^7 M_{\odot}$)	σ_{*}^{c} (km s^{-1})
RM 017	0.456	$56.6^{+7.3}_{-15.1}$	4509 ± 53	4569 ± 51	4159 ± 13	5604 ± 31	$23.1^{+4.7}_{-7.2}$	$103.1^{+21.2}_{-32.0}$	191.4 ± 3.7
RM 088	0.516	$54.8^{+2.9}_{-5.1}$	2449 ± 27	3320 ± 26	4451 ± 32	10290 ± 142	$11.8^{+2.0}_{-2.2}$	$52.7^{+8.9}_{-9.8}$	128.5 ± 12.3
RM 160	0.359	$21.0^{+1.4}_{-2.8}$	1707 ± 3	1318 ± 11	3805 ± 10	3642 ± 26	$0.7^{+0.1}_{-0.1}$	$3.2^{+0.6}_{-0.7}$...
RM 191	0.442	$16.7^{+4.1}_{-5.5}$	858 ± 6	796 ± 23	2050 ± 18	1575 ± 60	$0.2^{+0.1}_{-0.1}$	$0.9^{+0.3}_{-0.3}$	152.0 ± 8.5
RM 229	0.470	$22.1^{+7.7}_{-7.3}$	1528 ± 10	1738 ± 31	2271 ± 34	2103 ± 365	$1.3^{+0.5}_{-0.5}$	$5.8^{+2.2}_{-2.1}$	130.2 ± 8.7
RM 252	0.281	$10.1^{+2.4}_{-1.9}$	4300 ± 26	3384 ± 71	6574 ± 69	7868 ± 66	$2.3^{+0.6}_{-0.6}$	$10.1^{+2.9}_{-2.5}$	180.7 ± 4.0
RM 272	0.263	$32.2^{+15.6}_{-12.6}$	1408 ± 1	1298 ± 8	2436 ± 3	2632 ± 28	$1.1^{+0.5}_{-0.4}$	$4.7^{+2.4}_{-2.0}$...
RM 320	0.265	$20.2^{+10.5}_{-9.3}$	1538 ± 3	1320 ± 17	3232 ± 12	2808 ± 41	$0.7^{+0.4}_{-0.3}$	$3.1^{+1.7}_{-1.5}$	66.4 ± 4.6
RM 371	0.472	$22.6^{+0.6}_{-1.5}$	1381 ± 4	1346 ± 13	2678 ± 12	3483 ± 44	$0.8^{+0.1}_{-0.1}$	$3.6^{+0.6}_{-0.6}$...
RM 377	0.337	$5.7^{+0.5}_{-0.5}$	1407 ± 10	1372 ± 40	2802 ± 17	2971 ± 114	$0.2^{+0.0}_{-0.0}$	$0.9^{+0.2}_{-0.2}$	115.3 ± 4.6
RM 645	0.474	$24.2^{+10.2}_{-5.3}$	1378 ± 6	1352 ± 24	2825 ± 12	3118 ± 80	$0.9^{+0.4}_{-0.2}$	$3.9^{+1.7}_{-1.0}$...
RM 733	0.455	$53.0^{+8.7}_{-5.7}$	1488 ± 7	1590 ± 24	3284 ± 21	3489 ± 84	$2.6^{+0.6}_{-0.5}$	$11.7^{+2.7}_{-2.2}$	196.9 ± 16.6
RM 768	0.258	$42.1^{+2.7}_{-2.1}$	3428 ± 16	3232 ± 40	6213 ± 9	6279 ± 20	$8.6^{+1.5}_{-1.4}$	$38.3^{+6.6}_{-6.4}$	171.9 ± 2.8
RM 772	0.249	$5.9^{+1.6}_{-1.0}$	1104 ± 2	907 ± 6	2483 ± 9	2142 ± 11	$0.1^{+0.0}_{-0.0}$	$0.4^{+0.1}_{-0.1}$	136.5 ± 3.1
RM 776	0.116	$8.3^{+4.9}_{-2.3}$	1426 ± 2	1185 ± 7	2877 ± 6	2794 ± 15	$0.2^{+0.1}_{-0.1}$	$1.0^{+0.6}_{-0.3}$	112.4 ± 1.9
RM 779	0.152	$80.2^{+4.9}_{-6.3}$	1126 ± 2	1018 ± 7	2453 ± 5	2643 ± 23	$1.6^{+0.3}_{-0.3}$	$7.3^{+1.2}_{-1.3}$	57.1 ± 4.9
RM 790	0.237	$45.0^{+23.7}_{-3.9}$	3532 ± 17	5157 ± 40	5769 ± 18	8898 ± 66	$23.3^{+12.9}_{-4.1}$	$104.4^{+57.5}_{-19.0}$	204.4 ± 3.1
RM 840	0.244	$10.6^{+2.3}_{-2.4}$	3002 ± 45	3927 ± 30	4593 ± 14	6027 ± 19	$3.2^{+0.9}_{-0.9}$	$14.3^{+3.8}_{-4.0}$	164.3 ± 3.6

Notes.

^a Measurements are in the quasar rest frame. If the lag is detected by JAVELIN, we use the JAVELIN-reported lag by default; otherwise, we use the CREAM-reported lag.

^b Virial products were converted to M_{BH} using $f = 4.47$, as measured by Woo et al. (2015).

^c From Shen et al. (2015b).

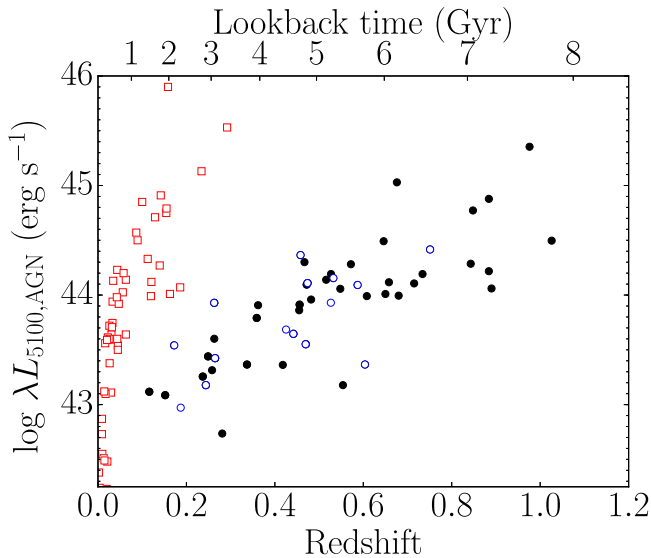


Figure 9. Distribution of redshift and $\log \lambda L_{5100}$ of the sources with detected $\text{H}\beta$ lags. Red open squares represent the 42 local RM AGNs compiled by Bentz & Katz (2015), with additions from Du et al. (2014, 2015) and Fausnaugh et al. (2017), showing average luminosities when multiple measurements exist for a single source. Blue open circles show the SDSS-RM first-lags sample from Shen et al. (2016b), and black solid circles show our new measurements. Note that the Shen et al. (2016b) measurements include Mg II detections and that there is overlap between eight of the Shen et al. (2016b) $\text{H}\beta$ measurements and our new measurements.

et al. (2015b), but they are also consistent with those measured independently by Matsuoka et al. (2015) based on a different spectral decomposition approach. Most of our measurements are consistent with the local quiescent $M_{\text{BH}}-\sigma_{*}$ relation, though large uncertainties and the presence of outliers at low σ_{*}

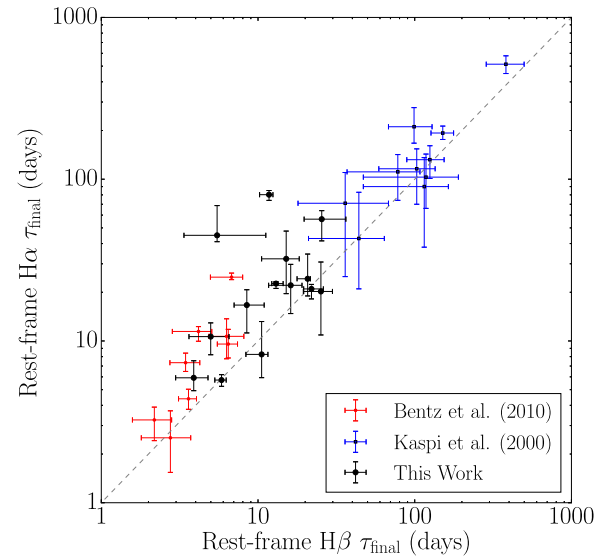


Figure 10. $\text{H}\alpha$ vs. $\text{H}\beta$ lag measurements for those objects where we detected significant lags for both emission lines (black solid circles). Red points represent measurements from Bentz et al. (2010), and blue squares represent measurements from Kaspi et al. (2000). The gray dashed line shows a ratio of one-to-one to guide the eye.

introduce a large amount of scatter and dilute any correlation within our sample. The four outliers at low σ_{*} are RMIDs 320, 338, 392, and 779. All four of these lag measurements appear solid: we see visible short-term variability in the light curves, and the lags are well determined, with clean posteriors. In addition, three out of the four lags are consistent with expectations from the $R-L$ relation, further suggesting that they are robust (the fourth source, RM 392, is expected to have

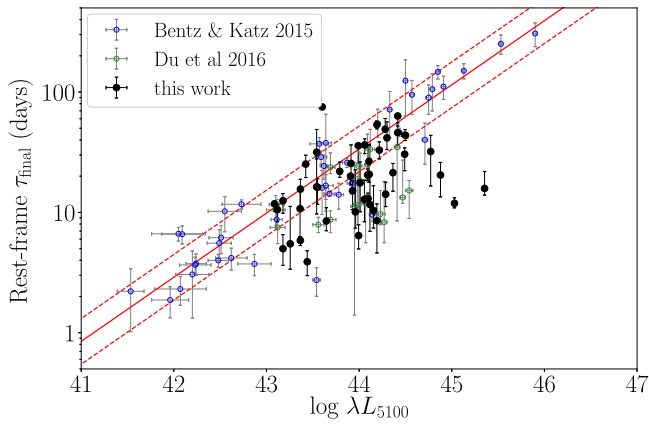


Figure 11. $H\beta$ R - L relationship, with previous measurements in blue (Bentz & Katz 2015) and green (Du et al. 2016b) and our new measurements in black. The red solid and dashed lines show the best-fit relation and its measured scatter from Bentz et al. (2013). Many of the SDSS-RM and Du et al. (2016b) lags lie below the main R - L relation: this may be (at least partly) due to selection effects from our limited monitoring cadence and duration, since our survey (and that of Du et al. 2016b) is not sensitive to long lags at high luminosities. The deviation may also be a physical effect associated with a different BLR size at high luminosities, or other quasar parameters that differ between the initial Bentz et al. (2013) data set and the SDSS-RM data and Du et al. (2016b) samples.

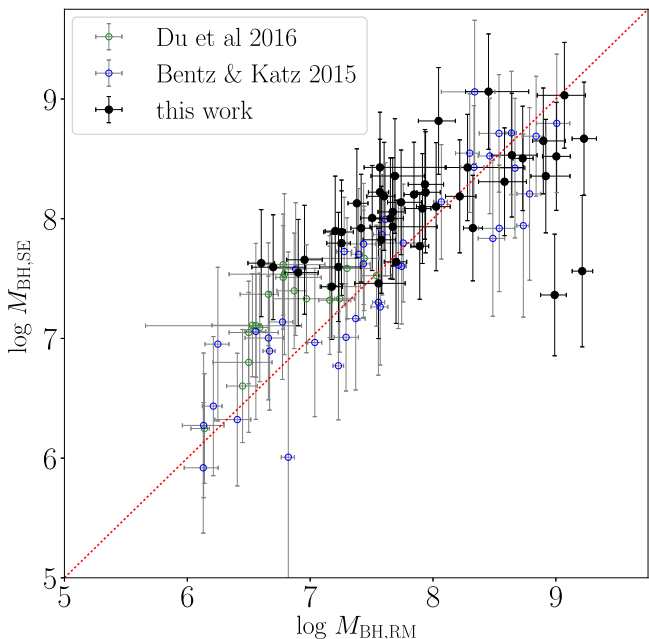


Figure 12. Comparison of $M_{\text{BH,SE}}$ measurements from Shen et al. (2015b) and our new measurements ($M_{\text{BH,RM}}$). As in Figure 11, we show previous measurements in blue (Bentz & Katz 2015) and green (Du et al. 2016b). The dotted red line indicates a ratio of one-to-one. Most of our quasars have consistent masses between the two methods, with some deviation for both SDSS-RM and the Du et al. (2016b) sample at low RM masses.

a much longer lag than we measure, however). Upon inspection, we find that there are likely issues with the σ_* measurements, all of which are below 100 km s^{-1} and approach the limits of the data used to measure them. We examined the spectral decomposition fits used to measure σ_* in these four sources and found that, using the Ca H/K lines only, the measurements for these sources are significantly higher, indicating that the original measurements are likely

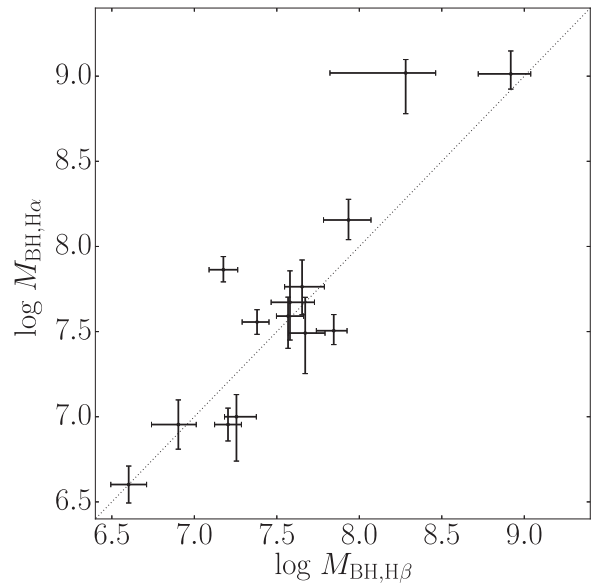


Figure 13. Comparison of M_{BH} measured from $H\beta$ and $H\alpha$ for those objects where we detected lags in both emission lines. The black dotted line shows a ratio of one-to-one.

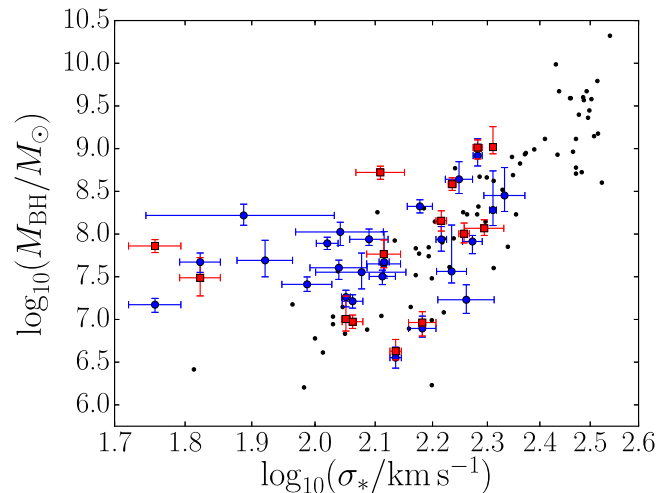


Figure 14. The $M_{\text{BH}}-\sigma_*$ relation with the sample of dynamical black hole masses from McConnell & Ma (2013) shown as black dots. Our new M_{BH} measurements made using the $H\beta$ and $H\alpha$ emission-line time lags and line widths are represented by blue circles and red squares, respectively.

underestimated; this is what causes them to appear as outliers on the $M_{\text{BH}}-\sigma_*$ relation.

4.3. Additional Sources of Systematics

When obtaining RM R_{BLR} measurements, RM studies often make the assumption that the time delay between the 5100 \AA continuum-emitting region and a relevant broad emission line (such as $H\beta$) is a good characterization of the distance between the BH and the $H\beta$ -emitting BLR. However, the R_{BLR} measured with RM is actually the distance between the optical continuum-emitting region and the BLR and not between the BLR and the BH itself; past RM efforts have generally assumed that the distance between the BH and the continuum-emitting region is negligible. Recent work has indicated that the optical continuum-emitting region can have a significant lag relative to the ultraviolet (Collier et al. 1998; Sergeev

et al. 2005; McHardy et al. 2014; Shappee et al. 2014; Edelson et al. 2015; Fausnaugh et al. 2016). Specifically, Fausnaugh et al. (2016) found that the V-band emitting region of NGC 5548 is 2 light-days farther out than the 1367 Å UV-emitting region in NGC 5548, a distance that is nonnegligible compared to the measured time lags for some of the broad emission lines (the He II λ 1640 emission line was measured to have a time delay of 2.4 days, for example). It is thus likely that our measurements of R_{BLR} using optical/BLR lags are underestimated.

Assuming a universal AGN accretion disk, where the distance between the UV and optical continuum-emitting regions is constant for all sources, a nonzero UV–optical time delay will not have an effect on RM M_{BH} measurements because the scale factor f automatically corrects, at least in a statistical sense, for this distance effect by requiring that AGNs fall on the quiescent $M_{\text{BH}}-\sigma_*$ relation. However, if the UV–optical distance depends on L or M_{BH} , this complication could pose a problem. Pei et al. (2017) examine possible dependencies on quasar parameters such as L and M_{BH} and report that the scaling with luminosity is expected to be slow. Microlensing studies also show that the size of the BLR more or less scales as expected with M_{BH} (Morgan et al. 2010; Mosquera et al. 2013).

In addition, the scatter in the $R-L$ relationship (Bentz et al. 2013) is small, so these effects are likely small for most AGNs, as a large UV–optical distance scaling would cause larger scatter in this relation. Thus far, there are only a few solid measurements of the UV–optical continuum time delay, so we are unable to directly measure any dependencies of UV–optical size with quasar properties. Additional measurements of interband continuum lags will be necessary to determine what (if any) correction is needed to account for the use of optical continua in measuring broad emission-line lags.

5. Summary

We have combined the spectroscopic and photometric observations from the first year of monitoring of the SDSS-RM program to search for significant time delays in 222 quasars. Our major findings are the following.

1. We have measured characteristic time delays between the continuum and the H β and H α broad emission lines in 44 and 18 sources, respectively. These measurements increase the size of the sample of AGNs that have reverberation mapping M_{BH} measurements by about two-thirds. In addition, most of these measurements are made for higher-redshift objects, significantly expanding the redshift coverage of the RM sample. See Section 4.
2. We compared three different methods of obtaining lag measurements: the ICCF, JAVELIN, and CREAM. All three methods are generally consistent with one another, though JAVELIN (32 H β and 13 H α lags) and CREAM (42 H β and 17 H α lags) typical yield smaller uncertainties and thus more high-significance detections than the ICCF (16 H β and eight H α lags). See Section 3.4.
3. We find that H α lags are generally consistent with or larger than the H β lags measured in the same sources, which is consistent with previous findings. See Section 4.1.
4. We find that many of our sources fall below the $R-L$ relation measured by Bentz et al. (2013). This could be due to selection effects or a dependency of the $R-L$

relation on accretion parameters such as the Eddington ratio. See Section 4.1.

5. We measure M_{BH} for those objects with successful lag detections. Most of our measurements are consistent with the $M_{\text{BH}}-\sigma_*$ relation measured in local quiescent galaxies, though we have some outliers at the low- σ_* end of the relation that are likely due to selection effects or issues with σ_* measurements. See Section 4.2.

With only the first year of data, we are sensitive only to lag measurements shorter than approximately 100 days in the observed frame. The next step is to incorporate the additional years of data from the SDSS-RM program to extend the lag sensitivity and the dynamic range in quasar luminosity. This will allow us to measure longer time delays and also will help remove aliases in our posterior lag distributions for shorter lags, which will likely reduce our false-positive rate. With the additional years of data that are already in hand or have been planned, we will also be able to investigate emission lines such as CIV and Mg II in higher-redshift targets, allowing us to probe quasars even farther out in the universe.

C.J.G., W.N.B., J.R.T., and D.P.S. acknowledge support from NSF grant AST-1517113. Y.S. acknowledges support from an Alfred P. Sloan Research Fellowship and NSF grant AST-1715579. C.S.K. is supported by NSF grant AST-1515427. K.H. acknowledges support from STFC grant ST/M001296/1. I.D.M. acknowledges support from NSF grant AST 15-15115. K.D.D. acknowledges support from the NSF awarded under NSF Grant AST-1302093. L.C.H. was supported by the National Key R&D Program of China (2016YFA0400702) and the National Science Foundation of China (11473002, 11721303).

This work is based on observations obtained with MegaPrime/MegaCam, a joint project of CFHT and CEA/DAPNIA, at the Canada–France–Hawaii Telescope (CFHT), which is operated by the National Research Council (NRC) of Canada, the Institut National des Sciences de l’Univers of the Centre National de la Recherche Scientifique of France, and the University of Hawaii. The authors wish to recognize and acknowledge the very significant cultural role and reverence that the summit of Maunakea has always had within the indigenous Hawaiian community. The astronomical community is most fortunate to have the opportunity to conduct observations from this mountain.






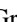






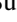









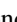
Funding for SDSS-III has been provided by the Alfred P. Sloan Foundation, the Participating Institutions, the National Science Foundation, and the U.S. Department of Energy Office of Science. The SDSS-III website is <http://www.sdss3.org/>.

SDSS-III is managed by the Astrophysical Research Consortium for the Participating Institutions of the SDSS-III Collaboration including the University of Arizona, the Brazilian Participation Group, Brookhaven National Laboratory, Carnegie Mellon University, University of Florida, the French Participation Group, the German Participation Group, Harvard University, the Instituto de Astrofísica de Canarias, the Michigan State/Notre Dame/JINA Participation Group, Johns Hopkins University, Lawrence Berkeley National Laboratory, Max Planck Institute for Astrophysics, Max Planck Institute for Extraterrestrial Physics, New Mexico State University, New York University, Ohio State University, Pennsylvania State University, University of Portsmouth, Princeton University, the Spanish Participation Group, University of Tokyo, University

of Utah, Vanderbilt University, University of Virginia, University of Washington, and Yale University.

We thank the Bok and CFHT Canadian, Chinese, and French TACs for their support. This research uses data obtained through the Telescope Access Program (TAP), which is funded by the National Astronomical Observatories, the Chinese Academy of Sciences, and the Special Fund for Astronomy from the Ministry of Finance in China.

ORCID iDs

C. J. Grier  <https://orcid.org/0000-0001-9920-6057>
 J. R. Trump  <https://orcid.org/0000-0002-1410-0470>
 Yue Shen  <https://orcid.org/0000-0003-1659-7035>
 Keith Horne  <https://orcid.org/0000-0003-1728-0304>
 Karen Kinemuchi  <https://orcid.org/0000-0001-7908-7724>
 Ian D. McGreer  <https://orcid.org/0000-0002-3461-5228>
 W. N. Brandt  <https://orcid.org/0000-0002-0167-2453>
 P. B. Hall  <https://orcid.org/0000-0002-1763-5825>
 C. S. Kochanek  <https://orcid.org/0000-0001-6017-2961>
 L. C. Ho  <https://orcid.org/0000-0001-6947-5846>
 B. M. Peterson  <https://orcid.org/0000-0001-6481-5397>
 Mouyuan Sun  <https://orcid.org/0000-0002-0771-2153>
 Dmitry Bizyaev  <https://orcid.org/0000-0002-3601-133X>
 Joel R. Brownstein  <https://orcid.org/0000-0002-8725-1069>
 Kevin Bundy  <https://orcid.org/0000-0001-9742-3138>
 K. S. Dawson  <https://orcid.org/0000-0002-0553-3805>
 Yang Gao  <https://orcid.org/0000-0002-6316-1632>
 Timothy A. Hutchinson  <https://orcid.org/0000-0002-3009-260X>
 Linhua Jiang  <https://orcid.org/0000-0003-4176-6486>
 Kaike Pan  <https://orcid.org/0000-0002-2835-2556>
 Kara A. Ponder  <https://orcid.org/0000-0002-8207-3304>
 Jesse Rogerson  <https://orcid.org/0000-0002-7078-1776>
 Audrey Simmons  <https://orcid.org/0000-0002-2364-7240>

References

- Ahn, C. P., Alexandroff, R., Allende Prieto, C., et al. 2014, *ApJS*, 211, 17
 Alard, C. 2000, *A&AS*, 144, 363
 Alard, C., & Lupton, R. H. 1998, *ApJ*, 503, 325
 Alexander, T. 1997, *Astrophysics and Space Science Library*, 218, 163
 Almaini, O., Lawrence, A., Shanks, T., et al. 2000, *MNRAS*, 315, 325
 Aune, S., Boulade, O., Charlot, X., et al. 2003, *Proc. SPIE*, 4841, 513
 Barth, A. J., Bennert, V. N., Canalizo, G., et al. 2015, *ApJS*, 217, 26
 Bentz, M. C., Denney, K. D., Grier, C. J., et al. 2013, *ApJ*, 767, 149
 Bentz, M. C., & Katz, S. 2015, *PASP*, 127, 67
 Bentz, M. C., Walsh, J. L., Barth, A. J., et al. 2009, *ApJ*, 705, 199
 Bentz, M. C., Walsh, J. L., Barth, A. J., et al. 2010, *ApJ*, 716, 993
 Blandford, R. D., & McKee, C. F. 1982, *ApJ*, 255, 419
 Blanton, M. R., Bershady, M. A., Abolfathi, B., et al. 2017, *AJ*, 154, 28
 Cameron, E. 2011, *PASA*, 28, 128
 Collier, S. J., Horne, K., Kaspi, S., et al. 1998, *ApJ*, 500, 162
 Dawson, K. S., Schlegel, D. J., Ahn, C. P., et al. 2013, *AJ*, 145, 10
 Denney, K. D., Horne, K., Shen, Y., et al. 2016, *ApJS*, 224, 14
 Denney, K. D., Peterson, B. M., Pogge, R. W., et al. 2010, *ApJ*, 721, 715
 Doi, M., Tanaka, M., Fukugita, M., et al. 2010, *AJ*, 139, 1628
 Du, P., Hu, C., Lu, K.-X., et al. 2014, *ApJ*, 782, 45
 Du, P., Hu, C., Lu, K.-X., et al. 2015, *ApJ*, 806, 22
 Du, P., Lu, K.-X., Hu, C., et al. 2016a, *ApJ*, 820, 27
 Du, P., Lu, K.-X., Zhang, Z.-X., et al. 2016b, *ApJ*, 825, 126
 Edelson, R., Gelbord, J. M., Horne, K., et al. 2015, *ApJ*, 806, 129
 Edelson, R. A., & Krolik, J. H. 1988, *ApJ*, 333, 646
 Eisenstein, D. J., Weinberg, D. H., Agol, E., et al. 2011, *AJ*, 142, 72
 Fausnaugh, M. M., Denney, K. D., Barth, A. J., et al. 2016, *ApJ*, 821, 56
 Fausnaugh, M. M., Grier, C. J., Bentz, M. C., et al. 2017, *ApJ*, 840, 97
 Fukugita, M., Ichikawa, T., Gunn, J. E., et al. 1996, *AJ*, 111, 1748
 Gaskell, C. M., & Peterson, B. M. 1987, *ApJS*, 65, 1
 Goad, M. R., Korista, K. T., De Rosa, G., et al. 2016, *ApJ*, 824, 11
 Grier, C. J., Hall, P. B., Brandt, W. N., et al. 2015, *ApJ*, 806, 111
 Grier, C. J., Peterson, B. M., Pogge, R. W., et al. 2012, *ApJ*, 755, 60
 Gunn, J. E., Siegmund, W. A., Mannery, E. J., et al. 2006, *AJ*, 131, 2332
 Hartman, J. D., Bakos, G., Stanek, K. Z., & Noyes, R. W. 2004, *AJ*, 128, 1761
 Hu, C., Du, P., Lu, K.-X., et al. 2015, *ApJ*, 804, 138
 Jiang, Y.-F., Green, P. J., Greene, J. E., et al. 2017, *ApJ*, 836, 186
 Kaspi, S., Brandt, W. N., Maoz, D., et al. 2007, *ApJ*, 659, 997
 Kaspi, S., Maoz, D., Netzer, H., et al. 2005, *ApJ*, 629, 61
 Kaspi, S., Smith, P. S., Netzer, H., et al. 2000, *ApJ*, 533, 631
 Kelly, B. C., Bechtold, J., & Siemiginowska, A. 2009, *ApJ*, 698, 895
 Korista, K. T., & Goad, M. R. 2004, *ApJ*, 606, 749
 Kozłowski, S. 2016, *MNRAS*, 459, 2787
 Kozłowski, S. 2017, *A&A*, 597, A128
 Kozłowski, S., Kochanek, C. S., Udalski, A., et al. 2010, *ApJ*, 708, 927
 Li, J., Shen, Y., Horne, K., et al. 2017, *ApJ*, 846, 79L
 MacLeod, C. L., Ivezić, Ž., Kochanek, C. S., et al. 2010, *ApJ*, 721, 1014
 MacLeod, C. L., Ivezić, Ž., Sesar, B., et al. 2012, *ApJ*, 753, 106
 Maronna, R. A., Martin, R. D., & Yohai, V. J. 2006, *Robust Statistics* (New York: Wiley)
 Matsuoka, Y., Strauss, M. A., Shen, Y., et al. 2015, *ApJ*, 811, 91
 McConnell, N. J., & Ma, C.-P. 2013, *ApJ*, 764, 184
 McHardy, I. M., Cameron, D. T., Dwelly, T., et al. 2014, *MNRAS*, 444, 1469
 Metzroth, K. G., Onken, C. A., & Peterson, B. M. 2006, *ApJ*, 647, 901
 Morgan, C. W., Kochanek, C. S., Morgan, N. D., & Falco, E. E. 2010, *ApJ*, 712, 1129
 Mosquera, A. M., Kochanek, C. S., Chen, B., et al. 2013, *ApJ*, 769, 53
 Netzer, H. 1975, *MNRAS*, 171, 395
 Onken, C. A., Ferrarese, L., Merritt, D., et al. 2004, *ApJ*, 615, 645
 Pei, L., Fausnaugh, M. M., Barth, A. J., et al. 2017, *ApJ*, 837, 131
 Peterson, B. M. 2011, in *Narrow-Line Seyfert 1 Galaxies and their Place in the Universe*, ed. L. Foschini et al. (Trieste: SISSA), 034
 Peterson, B. M., Ferrarese, L., Gilbert, K. M., et al. 2004, *ApJ*, 613, 682
 Rees, M. J., Netzer, H., & Ferland, G. J. 1989, *ApJ*, 347, 640
 Sergeev, S. G., Doroshenko, V. T., Golubinskiy, Y. V., Merkulova, N. I., & Sergeeva, E. A. 2005, *ApJ*, 622, 129
 Shappee, B. J., Prieto, J. L., Grupe, D., et al. 2014, *ApJ*, 788, 48
 Shen, Y., Brandt, W. N., Dawson, K. S., et al. 2015a, *ApJS*, 216, 4
 Shen, Y., Brandt, W. N., Richards, G. T., et al. 2016a, *ApJ*, 831, 7
 Shen, Y., Greene, J. E., Ho, L. C., et al. 2015b, *ApJ*, 805, 96
 Shen, Y., Horne, K., Grier, C. J., et al. 2016b, *ApJ*, 818, 30
 Shen, Y., Richards, G. T., Strauss, M. A., et al. 2011, *ApJS*, 194, 45
 Smee, S. A., Gunn, J. E., Uomoto, A., et al. 2013, *AJ*, 146, 32
 Starkey, D., Horne, K., Fausnaugh, M. M., et al. 2017, *ApJ*, 835, 65
 Starkey, D. A., Horne, K., & Villforth, C. 2016, *MNRAS*, 456, 1960
 Sun, M., Trump, J. R., Shen, Y., et al. 2015, *ApJ*, 811, 42
 Vestergaard, M., & Peterson, B. M. 2006, *ApJ*, 641, 689
 White, R. J., & Peterson, B. M. 1994, *PASP*, 106, 879
 Williams, G. G., Olszewski, E., Lesser, M. P., & Burge, J. H. 2004, *Proc. SPIE*, 5492, 787
 Woo, J.-H., Yoon, Y., Park, S., Park, D., & Kim, S. C. 2015, *ApJ*, 801, 38
 Zu, Y., Kochanek, C. S., Kozłowski, S., & Udalski, A. 2013, *ApJ*, 765, 106
 Zu, Y., Kochanek, C. S., & Peterson, B. M. 2011, *ApJ*, 735, 80